



# Benchmarking $K_{DP}$ in Rainfall: a Quantitative Assessment of Estimation Algorithms Using C-Band Weather Radar Observations

Miguel Aldana<sup>1</sup>, Seppo Pulkkinen<sup>1</sup>, Annakaisa von Lerber<sup>1</sup>, Matthew R. Kumjian<sup>2</sup>, and Dmitri Moisseev<sup>1,3</sup>

<sup>1</sup>Space Research & Observation Technologies, Finnish Meteorological Institute, Helsinki, Finland

<sup>2</sup>Department of Meteorology & Atmospheric Science, The Pennsylvania State University, Pennsylvania, United States

<sup>3</sup>Institute for Atmospheric & Earth system Research, University of Helsinki, Helsinki, Finland

**Correspondence:** Miguel Aldana (miguel.aldana@fmi.fi)

**Abstract.** Accurate and precise  $K_{DP}$  estimates are essential for radar-based applications, especially in quantitative precipitation estimation and radar data quality control routines. The accuracy of these estimates largely depends on the post-processing of the radar's measured  $\Phi_{DP}$ , which aims to reduce noise and backscattering effects while preserving fine-scale precipitation features. In this study, we evaluate the performance of several publicly available  $K_{DP}$  estimation methods implemented in open-source libraries such as PyArt and Wradlib, and the method used in the Vaisala weather radars. To benchmark these methods, we employ a polarimetric self-consistency approach that relates  $K_{DP}$  to reflectivity and differential reflectivity in rain, providing a reference self-consistency  $K_{DP}$  ( $K_{DP}^{sc}$ ) for comparison. This approach allows for the construction of the reference  $K_{DP}$  observations that can be used to assess the accuracy and robustness of the studied  $K_{DP}$  estimation methods. We assess each method by quantifying uncertainties using C-band weather radar observations where the reflectivity values ranged between 20 and 50 dBZ.

Using the proposed evaluation framework we could define optimized parameter settings for the methods that have user-configurable parameters. Most of such methods showed significant reduction in the estimation errors after the optimization with respect to the default settings. We have found significant differences in the performances of the studied methods, where the best performing methods showed smaller normalized biases in the high reflectivity values (i.e.,  $\geq 40$  dBZ) and overall smaller normalized root mean squared errors across the range of reflectivity values.

## 1 Introduction

The specific differential phase ( $K_{DP}$ ) plays an important role in many weather radar applications, particularly in hydrometeor classification (Vivekanandan et al., 1999; Liu and Chandrasekar, 2000; Zrnić et al., 2001; Keenan, 2003; Lim et al., 2005; Tessendorf et al., 2005; Marzano et al., 2007; Dolan and Rutledge, 2009; Park et al., 2009; Snyder et al., 2010; Al-Sakka et al., 2013; Dolan et al., 2013; Thompson et al., 2014; Bechini and Chandrasekar, 2015; Grazioli et al., 2015; Wen et al., 2015; Besic et al., 2016; Ribaud et al., 2019) and quantitative precipitation estimation (QPE) (Sachidananda and Zrnić, 1987; Chandrasekar et al., 1990; Ryzhkov and Zrnić, 1995, 1996; May et al., 1999; Bringi and Chandrasekar, 2001; Bringi et al., 2006; Matrosov et al., 2006; Giangrande and Ryzhkov, 2008; Bringi et al., 2011; Cifelli et al., 2011; Wang et al., 2013; Chen and Chandrasekar,



2015; Chen et al., 2017; Thompson et al., 2018; Zhang et al., 2020), and is used in data assimilation for numerical weather prediction models (Thomas et al., 2020; Du et al., 2021) and in hydrological applications (Brandes et al., 2002; Ryzhkov et al., 2005b; Vulpiani et al., 2012; Li et al., 2023; Cremonini et al., 2023). Compared to radar power variables, i.e., reflectivity factor at horizontal polarization ( $Z_H$ ) and differential reflectivity ( $Z_{dr}$ ),  $K_{DP}$  offers advantages in terms of accuracy, resilience, and reliability due to its immunity to radar miscalibration, attenuation (Bringi and Chandrasekar, 2001; Illingworth, 2004; Ryzhkov and Zrníc, 2019), and partial beam blockage (Zrníc and Ryzhkov, 1996). It has also proven successful in hydrometeor classification routines (Lim et al., 2005; Park et al., 2009; Grazioli et al., 2015; Tiira and Moisseev, 2020), especially in the detection of graupel (Dolan and Rutledge, 2009; Oue et al., 2015), small melting hail (Kumjian et al., 2019), and dendritic growth zone and processes within (Kennedy and Rutledge, 2011; Andrić et al., 2013; Schneebeli et al., 2013; Moisseev et al., 2015; Kumjian and Lombardo, 2017). The ability of  $K_{DP}$  to accurately estimate heavy rainfall, differentiate hydrometeor types, and overcome attenuation in precipitation makes it an invaluable operational and research radar variable.

35  
Despite its advantages, accurate estimation of  $K_{DP}$  from radar-measured differential phase ( $\Phi_{DP}$ ) remains challenging. Mathematically,  $K_{DP}$  is half the range derivative of  $\Phi_{DP}$ , which measures the phase shift between horizontally and vertically polarized signals as they propagate through precipitation. This phase shift ( $\Phi_{DP}$ ) is influenced by hydrometeor concentration, shape, orientation, and composition (Kumjian, 2018). However,  $\Phi_{DP}$  is not typically smooth and monotonically increasing along the rain path; it contains fluctuations due to noise ( $\epsilon$ ) and backscattering differential phase ( $\delta_{HV}$ ) (Ryzhkov and Zrníc, 1996; Ryzhkov and Zrníc, 1998). Excessive filtering of  $\Phi_{DP}$  to remove  $\epsilon$  can lead to the loss of fine-scale precipitation features, affecting the accuracy of  $K_{DP}$  estimates especially in light precipitation (Huang et al., 2017). In heavier precipitation,  $\delta_{HV}$  causes spikes in  $\Phi_{DP}$ , especially at higher radar frequencies, further complicating accurate  $K_{DP}$  estimation (Bringi and Chandrasekar, 2001).

45  
To address these challenges, various methods have been developed to post-process  $\Phi_{DP}$  and derive  $K_{DP}$  (Hubbert et al., 1993; Hubbert and Bringi, 1995; Ryzhkov et al., 2005c; Wang and Chandrasekar, 2009; Otto and Russchenberg, 2011; Maesaka et al., 2012; Vulpiani et al., 2012; Schneebeli and Berne, 2012; Giangrande et al., 2013; Schneebeli et al., 2014; Huang et al., 2017; Reinoso-Rondinel et al., 2018; Wen et al., 2019). Basic approaches include median filters and moving windows, while more advanced methods use regression techniques and self-consistency constraints based on  $Z_H$  or  $Z_{dr}$ . Many of these methods are now available in open-source Python libraries such as PyArt (Helmus and Collis, 2016) and Wradlib (Heistermann et al., 2013). For this study, some of the most popular implemented methods based on Maesaka et al. (2012), Vulpiani et al. (2012), Giangrande et al. (2013), and Schneebeli et al. (2014) were selected for analysis. Additionally, the  $K_{DP}$  product implemented by Vaisala in IRIS software (Vaisala, 2017) based on Wang and Chandrasekar (2009) was also included in our analysis. Each algorithm has its own data requirements, mathematical approach, and optimizing parameters, raising the question of which performs optimally under varying parameter settings, and rainfall intensities.

Recent studies show that  $K_{DP}$  estimates can vary significantly depending on the algorithm and the optimizing parameters



used. Reimel and Kumjian (2021) evaluated the errors of several methods using synthetic  $K_{DP}$  profiles and found that no  
60 single algorithm was optimal across all rainfall conditions. Instead, performance varied with the complexity of the rain profile  
and selected parameters. They identified `kdp_maesaka` (PyArt’s implementation of Maesaka et al. (2012)) and `phase_proc_lp`  
(PyArt’s implementation of Giangrande et al. (2013)) as particularly versatile. However, Reimel and Kumjian (2021) used  
synthetic data, which may miss some of the effects present in radar observations of rainfall (e.g.,  $\delta_{HV}$ ). More recently, Li et al.  
(2023) compared `kdp_maesaka` and `phase_proc_lp` in an extreme summer rainfall event, finding that fine-tuning the methods  
65 played a key role in retrieving the most accurate  $K_{DP}$  estimate. Despite these insights, the performance and uncertainties of  
most methods in rainfall observations remain largely unexplored.

The goal of this study is to evaluate the performance of publicly available  $K_{DP}$  estimation methods in real rainfall obser-  
vations and quantify their uncertainties as a function of reflectivity intensities. We use self-consistency relations linking  $K_{DP}$   
70 to  $Z_H$  and  $Z_{dr}$  to compute benchmark  $K_{DP}$  profiles (herein  $K_{DP}^{sc}$ ), requiring thorough selection and filtering of data.  $K_{DP}^{sc}$   
computed from quality-controlled  $Z_H$  and  $Z_{dr}$  measurements provides a solid benchmark against which to compare the meth-  
ods’ performances, select optimal parameters, and quantify the associated uncertainties.

This paper is organized as follows: Section 2 describes the radar and disdrometer data, the evaluation framework, and intro-  
75 duces the  $K_{DP}$  estimation methods. Section 3 presents and discusses the parameter optimization and performance evaluation  
of the methods, and Section 4 summarizes the findings.

## 2 Data & Methods

### 2.1 Radar & Disdrometer Data

This study evaluates the performance of  $K_{DP}$  estimation methods using real rainfall data. The dataset was collected from the  
80 Finnish Meteorological Institute’s (FMI) C-band Vantaa radar, located near Helsinki, Finland (see Fig. 1). The radar recorded  
various quantities, including  $Z_H$ ,  $Z_{dr}$ ,  $\Phi_{DP}$ ,  $K_{DP}$ , cross-correlation coefficient ( $\rho_{HV}$ ), and the hydrometeor classification  
product available in IRIS (Vaisala, 2017) and based on the methodology described by Chandrasekar et al. (2013). The spatial  
resolution of the radar is 500 meters in range and  $1^\circ$  in azimuth, with scans performed every 5 minutes, and the data was  
collected with an elevation angle of  $0.7^\circ$ . The dataset spans from June to September during the years 2017 to 2019, capturing  
85 precipitation events with variable rainfall intensities and spatial extents. The raw radar dataset as well as the post-processed  
 $K_{DP}$  estimates are available from the link provided in Aldana (2024).

To ensure data quality, only periods when the Vantaa radar had calibration errors within 1 dB were selected. The calibra-  
tion was verified by i) identifying periods where solar flux estimates from Vantaa radar estimates aligned consistently with  
90 Dominion Radio Astrophysical Observatory (DRAO) estimates (Huuskonen and Holleman, 2007; Tapping, 2013; Holleman  
et al., 2022), and ii) selecting radar scans within these periods where  $Z_H$ -calibration offsets were within 1 dB, following the



**Figure 1.** Map showing locations of FMI’s Vantaa radar (VAN) and Hyytiälä’s research station where DSD data were collected. The shaded area is a circle of 250 km radius corresponding to the spatial coverage of the radar.

absolute calibration procedure outlined by (Gourley et al., 2009).  $Z_{dr}$  bias was estimated and corrected during these periods by computing the offset between observed and self-consistency  $Z_{dr}$ , derived from observed  $Z_H$ , as described in (Hickman, 2015) and computing the average for several cases.

95

The performance of the  $K_{DP}$  estimation methods is benchmarked against self-consistency  $K_{DP}^{sc}$ , computed from measured  $Z_H$ ,  $Z_{dr}$  and using self-consistency relations. These relations, which link the polarimetric radar variables, have been widely used for radar calibration correction (Gorgucci et al., 1992; Goddard et al., 1994; Illingworth and Blackman, 2002; Vivekanandan et al., 2003; Ryzhkov et al., 2005a). The self-consistency relations were derived by fitting radar variables computed using  
100 the open-source library, PyTMatrix (Leinonen, 2014). PyTMatrix provides a simple interface for T-Matrix electromagnetic scattering calculations (Waterman, 1965; I. Mishchenko et al., 2000), requiring the user to provide drop size distribution (DSD) data and setting parameters such as temperature, radar wavelength’s band and raindrop shape model. The settings applied were 10°C, C-band and Thurai et al. (2007), respectively, and the DSD data provided was collected by an optical Parsivel disdrometer (Moisseev, 2024) located in Hyytiälä, Finland (see Fig. 1).

105

The Parsivel disdrometer records the number of particles and velocity at one-minute intervals, sorting the data into 32 bins depending on particle’s size (i.e., equivalent volume diameter) and 32 additional bins depending on particle’s fall velocity. From the number of particles, size and velocity classes, the Parsivel disdrometer computes the precipitation type, which was used to filter out non-liquid particles. Observations were further limited to times when the 30-minute average 2-meter tem-





110 perature exceeded 2°C to ensure liquid rain only. Following the filtering procedure to reduce statistical errors suggested by  
Leinonen et al. (2012), only those measurements with at least 100 counts in two consecutive bins and positive counts in at  
least four consecutive bins were retained. The disdrometer dataset, covering June to September from 2014 to 2019, provided  
a robust basis for deriving average summer-season DSD parameters such as mean volume diameter ( $D_0$ ), intercept parameter  
( $N_w$ ), and shape parameter ( $\mu$ ). These parameters showed strong agreement with those reported by Leinonen et al. (2012) in  
115 a climatological study of Finland. From the derived DSD parameters ( $N_w$ ,  $D_0$ , and  $\mu$ ), the polarimetric radar variables were  
computed and used for deriving the self-consistency relation defining the framework to evaluate the  $K_{DP}$  estimation methods.

## 2.2 $K_{DP}$ Evaluation Framework

The performance of  $K_{DP}$  estimation methods is evaluated using  $K_{DP}^{sc}$  as benchmark. This quantity is calculated from each  
radar-measured tuple ( $Z_H$ ,  $Z_{dr}$ ) following a relationship of the form (Gourley et al., 2009):

$$120 \quad K_{DP}^{sc} = z_H \times 10^{-5} \times (a_1 + a_2 \times Z_{dr} + a_3 \times Z_{dr}^2 + a_4 \times Z_{dr}^3), \quad (1)$$

where  $z_H = 10^{0.1 \times Z_H}$  represents  $Z_H$  in linear units ( $\text{mm}^6 \text{m}^{-3}$ ) and  $Z_{dr}$  is in decibels (dB). The coefficients used in this re-  
lation are  $a_1 = 6.78$ ,  $a_2 = -2.65$ ,  $a_3 = 0.562$  and  $a_4 = -0.0624$ . The coefficients align well with those reported by Gourley  
et al. (2009), which employed the raindrop shape models by Brandes et al. (2002) and Thurai and Bringi (2005).

125 To ensure the accuracy and robustness of  $K_{DP}^{sc}$  estimates used in the method assessment, it was crucial to quality-control  
the  $Z_H$  and  $Z_{dr}$  data. Radar observations of rain are often affected by non-meteorological measurements, resonance effects,  
and hail contamination (Bringi and Chandrasekar, 2001; Kumjian, 2013; Ryzhkov and Zrnica, 2019). To address these issues,  
the following filtering steps were applied:

- *Noise filtering*: A minimum threshold of 0.97 was applied to  $\rho_{HV}$ .
- 130 – *Non-meteorological observations filtering*: The hydrometeor classification product from IRIS (Vaisala, 2017), based on  
Chandrasekar et al. (2013), was used to exclude gates classified as non-meteorological.
- $\delta_{HV}$  reduction: Gates with  $Z_{dr} > 3.5$  dB were excluded (Bringi and Chandrasekar, 2001; Gourley et al., 2009).
- *Non-liquid rain filtering*:
  - Only radar scans from the warm months (Jun-Sep) were selected.
  - 135 – Gates not classified as rain by the hydrometeor classification product were excluded.
  - Hail contamination was addressed by removing gates with  $Z_H \geq 50$  dBZ.
  - Observations from the melting layer and above were suppressed by masking gates farther than 70 km (see last  
dashed ring in Fig. 2) from the radar in the radial direction. The distance was manually set by identifying gates  
with melting layer signatures (Giangrande et al., 2008; Boodoo et al., 2010).

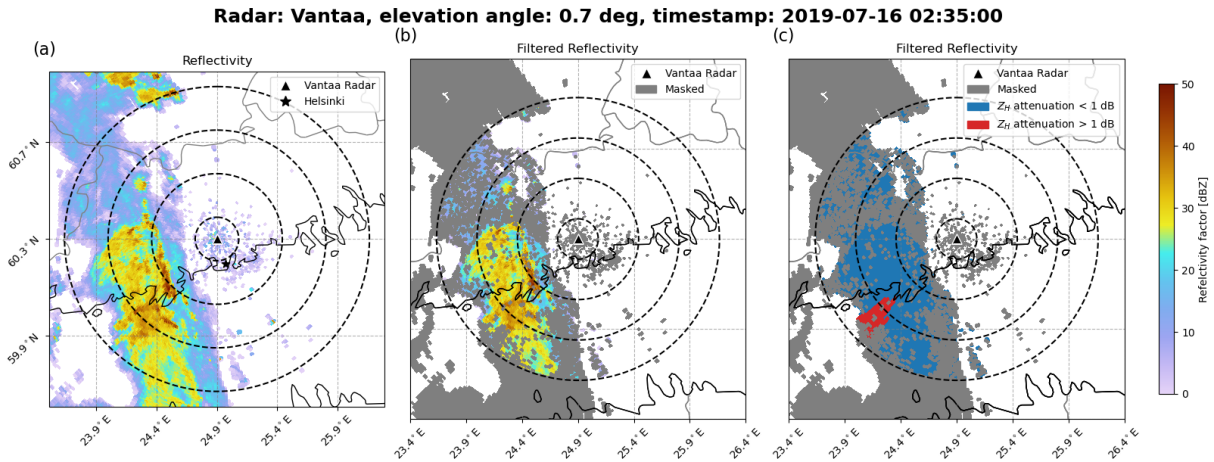


**Figure 2.** Example of a Vantaa radar scan during a precipitation event on the 16 July 2019 at an elevation angle of  $0.7^\circ$ . Panel (a) shows measured  $Z_H$ ; panel (b) shows filtered  $Z_H$  with masked gates in grey; panel (c) shows the same as (b) but with attenuated gates marked in red and non-attenuated gates marked in blue. Dashed rings represent radial distances of 10, 30, 50 and 70 km from the radar.

140 In addition to addressing noise and non-liquid rain measurements,  $K_{DP}^{sc}$  estimates are affected by attenuation in  $Z_H$  and differential attenuation in  $Z_{dr}$ , particularly in cases of heavy rainfall, extended propagation paths through rain (hereafter “rain paths”) (Zrnić and Ryzhkov, 1996; Carey et al., 2000; Bringi and Chandrasekar, 2001; Kumjian, 2013), and when the radar’s antenna radome is wet (Blevis, 1965; Kurri and Huuskonen, 2008). To mitigate these effects, radar scans when there was rain on top of the radar within the past 20 minutes were discarded. Then, for the remaining cases, attenuation in heavy precipitation or extended rain paths were addressed by flagging the radar gates when suspected attenuation of at least 1 dB was detected.

145 The attenuation in range gates was inferred using a standard method that linearly relates the losses in  $Z_H$  and  $Z_{dr}$  with increases in  $\Delta\Phi_{DP}$  (Ryzhkov and Zrnić, 1995; Carey et al., 2000; Bringi and Chandrasekar, 2001; Gourley et al., 2009).  $\Delta\Phi_{DP}$  corresponds to the total span of  $\Phi_{DP}$  along the radial within a rain path. A rain path was defined as a set of consecutive gates with rain features extending at least 20 km in the radial direction. For C-band radar, a minimum threshold of  $12^\circ$  in  $\Delta\Phi_{DP}$  indicates attenuation of at least 1 dB (Carey et al., 2000). In this study, a threshold of  $10^\circ$  was used, meaning that gates within rain paths featuring  $\Delta\Phi_{DP} \geq 10^\circ$  were flagged as attenuated.

150

An example of the filtering procedure applied to a radar scan is shown in Fig. 2. This figure demonstrates the effects of the filtering process and considered attenuation on the chosen data samples.

155

Following the filtering process, the dataset comprised 652,624 quality-controlled gates from 70 radar scans. Figure 3 presents a histogram of the data proportions across different  $Z_H$  values, showing the highest percentage of data between 30-35 dBZ, with a sharp decrease from 35-50 dBZ. The stacked bars indicate the percentages of attenuated and non-attenuated gates, with

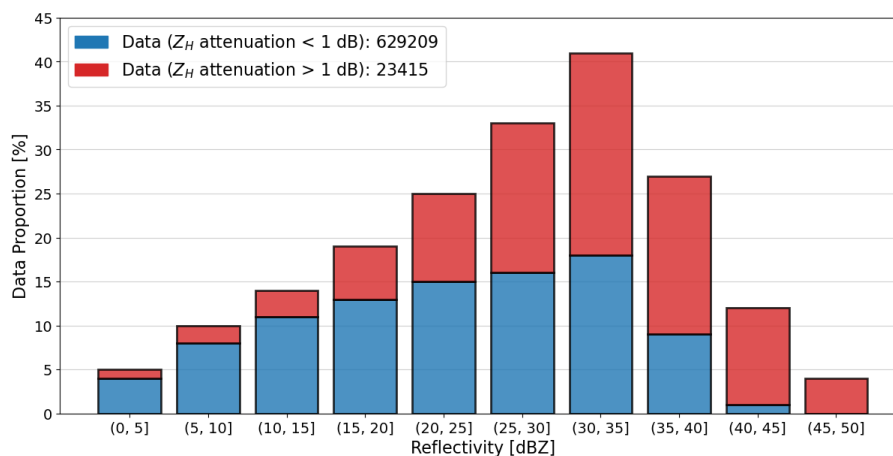


**Figure 3.** Proportion of data across  $Z_H$  intervals of 5 dBZ. Attenuated data is represented by red bars and non-attenuated data is represented by blue bars. The legend indicates the total number of gates with suspected attenuation of at least 1 dB (red) and less than 1 dB (blue).

the ratio of attenuated to non-attenuated data increasing with greater  $Z_H$ .

160

### 2.3 $K_{DP}$ Estimation methods

This Section provides an overview of the  $K_{DP}$  estimation methods selected for this study. The selection criteria focused on the availability of these methods in widely used open-source libraries, such as PyArt (Helmus and Collis, 2016) and Wradlib (Heistermann et al., 2013). At the time of this study, PyArt version 1.17.0 included the following methods: `kdp_maesaka`,  
 165 `kdp_vulpiani`, `phase_proc_lp` and `kdp_schneebeli`. Wradlib version 2.0.3 included `kdp_from_phidp` and `phidp_kdp_vulpiani`. However, `phidp_kdp_vulpiani` was excluded from our analysis, as it is based on the same method proposed by Vulpiani et al. (2012) that is already represented by PyArt in `kdp_vulpiani`. Additionally, `kdp_iris`, a method based on Wang and Chandrasekar (2009) and implemented by Vaisala in the IRIS software (Vaisala, 2017) was included. Table 1 summarizes the key features of the selected methods and a brief description of the methods is provided below.

170 a. **`kdp_maesaka`**. Developed by Maesaka et al. (2012) and available in PyArt, this method estimates non-negative  $K_{DP}$  from liquid precipitation measurements. It addresses the issue of negative  $K_{DP}$  estimates observed in exclusively liquid precipitation regions when using classical methods based on iterative filtering and local linear regression. Maesaka et al. (2012) identified that negative  $K_{DP}$  were caused by noise in  $\Phi_{DP}$  during weak precipitation and  $\delta_{HV}$  during heavy precipitation. The method restricts  $K_{DP}$  to positive values and assumes that  $\Phi_{DP}$  is a monotonically increasing function  
 175 with range, already unfolded.

b. **`kdp_vulpiani`**. Developed by Vulpiani et al. (2012) and available in PyArt, this method estimates  $K_{DP}$  for any type of precipitation. It uses a multistep, moving-window range derivative approach to obtain  $K_{DP}$ . It calculates a  $K_{DP}$



**Table 1.** List of  $K_{DP}$  methods studied with key features.

Method	Source	Data pre-requisites	Precipitation Type	Mathematical Approach (constraints)	Tested Parameters
kdp_maesaka	PyArt	Unfolded $\phi_{DP}$	liquid	Variational	<i>clpf</i>
kdp_vulpiani	PyArt	Pre-filtered $\Psi_{DP}$	Any	Moving window	<i>windsize, n_iter</i>
phase_proc_lp	PyArt	Unattenuated $Z_H$	liquid	Linear Programming ( $K_{DP}(Z_H)$ )	<i>self_const, coef, win- dow_len</i>
kdp_from_phidp	Wradlib	No NaN values	Any	Moving window	<i>winlen, dr</i>
kdp_schneebeli	PyArt	Pre-filtered $\Psi_{DP}$	Any	Kalman filter	-
kdp_iris	IRIS	-	Any	Adaptive regression	-

profile from the range derivative of a noise-reduced, offset-corrected, and unfolded  $\Phi_{DP}$  profile. At each window,  $K_{DP}$  is compared to thresholds representing unrealistic  $K_{DP}$  values within precipitation, correcting possible aliasing with the minimum threshold.

180

c. **phase\_proc\_lp**. Developed by Giangrande et al. (2013) and available in PyArt, this method estimates non-negative  $K_{DP}$  from liquid precipitation measurements. It uses a linear-programming (LP) method to enforce monotonic behavior in  $\Phi_{DP}$ , restricting  $K_{DP}$  to positive values. It extracts  $\delta_{HV}$  from  $\Phi_{DP}$  and it uses self-consistency constraints to bound  $K_{DP}$  estimates based on measured  $Z_H$ . The method requires quality-controlled  $Z_H$  and allows user-defined thresholds to exclude hail and set the environmental 0 °C level to exclude mixed-phase particles.

185

d. **kdp\_from\_phidp**. Implemented in wradlib (Heistermann et al., 2013) based on Vulpiani et al. (2012), this method estimates  $K_{DP}$  for any type of precipitation. It computes range-wise differentiation of  $\Phi_{DP}$  over a user-defined window size length, defaulting to 7 gates for a range resolution of 1 km. Unlike kdp\_vulpiani, it allows the selection of the method for range-gate differentiation, albeit it does not support multiple iterations, prioritizing speed over phase unfolding and noise issues in  $\Phi_{DP}$ .

190

e. **kdp\_schneebeli**. Developed by Schneebeli et al. (2014) and available in PyART, this method estimates  $K_{DP}$  for any type of precipitation. It selects the best-averaged  $K_{DP}$  profile from forward and backward propagation Kalman-filtered estimates. The Kalman filters are applied twice to each range gate state (accounting for forward and backward propagation) multiple times, recalculating the covariance matrices each time to yield unique states, and the best estimate is selected.

195

f. **kdp\_iris**. Implemented in the Vaisala’s software IRIS (Vaisala, 2017) and based on Wang and Chandrasekar (2009), this method estimates  $K_{DP}$  for any type of precipitation. It computes  $K_{DP}$  adaptively through piece-wise regression and a regularization framework that minimizes both smoothness in  $\Phi_{DP}$  and regression errors. The regularization adapts based



200 on range variations in  $K_{DP}$  and  $\rho_{HV}$  measurements, preserving steep  $\Phi_{DP}$  changes in high-intensity precipitation while reducing variations in low-intensity precipitation.

### 3 Results

#### 3.1 Parameter Optimization of methods

In this Section, we optimize the methods `kdp_maesaka`, `kdp_vulpiani`, `phase_proc_lp` and `kdp_from_phidp`, by quantifying the errors under varying parameter settings, and selecting the optimal values. First, a qualitative analysis is provided with the use of  $K_{DP}$  vs.  $Z_H$  scatter plots, illustrating the relationship between estimated  $K_{DP}$  (y-axis) and  $Z_H$  (x-axis), and benchmarking against  $K_{DP}^{sc}$  (dashed black line). Then, the errors of each method as a function of parameter setting and  $Z_H$  is provided. To achieve this, the dataset was divided into six 5-dB intervals ranging from 20 to 50 dBZ; we then computed for each interval the root mean square error (RMSE) and mean error (herein bias) and normalized by the mean  $K_{DP}^{sc}$  from each interval. The optimal parameters were selected based on the smallest averaged normalized RMSE (herein NRMSE) in the last three  $Z_H$  intervals (i.e., 35-50 dBZ), prioritizing the accuracy of  $K_{DP}$  estimates in high-intensity precipitation.

##### 3.1.1 PyArt's Maesaka method

PyArt's implementation of Maesaka et al. (2012), `kdp_maesaka`, features the optimizing parameter  $Clpf$ , which regulates the low-pass filter in  $\Phi_{DP}$ . The low-pass filter controls the degree of smoothing of  $\Phi_{DP}$ , with higher  $Clpf$  values producing smoother  $\Phi_{DP}$  profiles. In `kdp_maesaka`, the default value of  $Clpf$  is 1.0, and this value is scaled by the range resolution of the radar to match the resolution of the constraints applied to  $\Phi_{DP}$ . The scaling is proportional to the fourth power of the range resolution of the radar, and if we were to compare to the values used in Maesaka et al. (2012), a value of 1.0 corresponds to  $10^{10}$  for Vantaa radar's range resolution of 500 m. In Maesaka et al. (2012),  $Clpf$  values from  $10^9$  to  $10^{13}$  were tested on one rainfall case using a 250-m range resolution X-band radar. Their results show that values closer to  $10^{13}$  suppressed fine-scale precipitation features while producing a smooth and clean  $K_{DP}$ , whereas values closer to  $10^9$  preserved fine-scale features while substantially including more noise. These results lead us to test values from  $10^8$  to  $10^{15}$ , corresponding to  $10^{-2}$  and  $10^5$  in `kdp_maesaka` accounting for Vantaa's radar range resolution. Figure 4 shows scatter plots of  $K_{DP}$  estimates using `kdp_maesaka` as a function of  $Z_H$  for different  $Clpf$  values. All scatter plots show overall accurate and precise  $K_{DP}$  estimates within the  $Z_H$  range 0-30 dBZ. This result implies that the subset of  $Clpf$  values studied produce sufficiently smoothed  $\Phi_{DP}$  to reduce the impact of noise in light precipitation. However, the effects of excessive smoothing are observed at the range of 40-50 dBZ, where  $K_{DP}$  noticeably underestimates  $K_{DP}^{sc}$ . By comparing the scatter plots from  $Clpf = 10^{-2}$  to  $Clpf = 10^5$  in the  $Z_H$  interval 40-50 dBZ, the underestimation of  $K_{DP}$  is stronger with increasing  $Clpf$ .

To capture the influence of  $Clpf$  on the errors when estimating  $K_{DP}$  as a function of precipitation intensity, Figs. 5(a) and 5(b) show NRMSE and normalized bias of  $K_{DP}$  estimates with varying  $Clpf$ . The smaller and consistent NRMSEs in regions

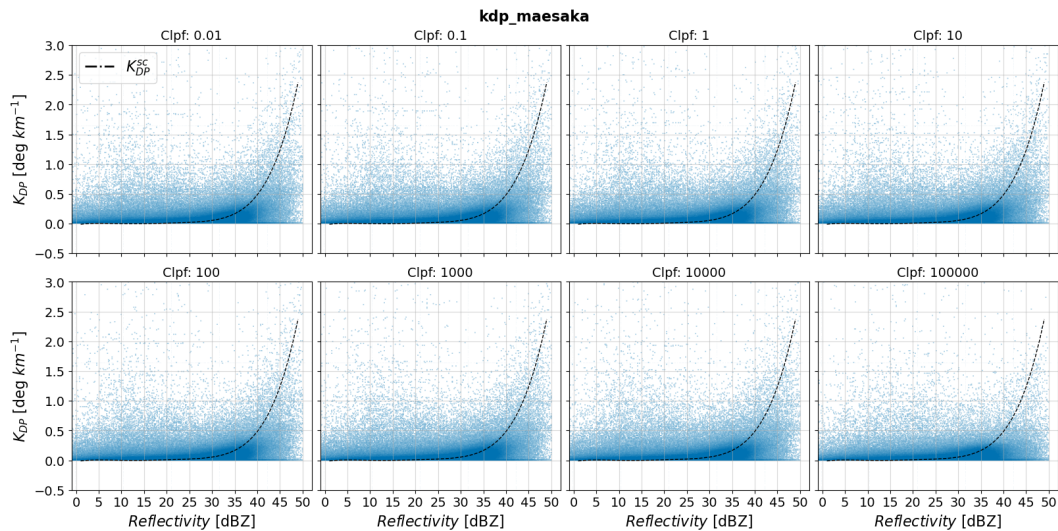


**Figure 4.** Scatter plots of estimated  $K_{DP}$  from `kdp_maesaka` as function of reflectivity and for various values of  $Clpf$ . Panels (a)-(h) show results with  $Clpf$  values from  $10^{-2}$  to  $10^5$ . The dashed black line corresponds to  $K_{DP}^{sc}$ .

230 of  $Z_H \geq 35$  dBZ in Fig. 5(a) indicate that `kdp_maesaka` reaches stable solutions for all  $Clpf$  values tested. However,  $Clpf$  of  $10^5$  showed the largest variability when transitioning from lowest to highest  $Z_H$  among the values tested, producing largest NRMSE for  $Z_H \geq 35$  dBZ and lowest otherwise. The underestimation of  $K_{DP}$  using  $10^5$  is evidenced in Fig. 5(b) for  $Z_H \geq 35$  dBZ, where the results were the most negatively biased, whereas the results when from the remaining parameters produced consistent NRMSE values that were much smaller.

235

Our results show that larger values of  $Clpf$  lead to larger errors due to oversmoothing in  $\Phi_{DP}$ . Overall, `kdp_maesaka` performs consistently when precipitation intensities reach 35 dBZ. The  $Clpf$  yielding the smallest 35-50-dBZ-averaged NRMSE was  $10^{-2}$ .

### 3.1.2 PyArt's Vulpiani method

240 PyArt's implementation of Vulpiani et al. (2012), `kdp_vulpiani`, features two optimizing parameters: *windsize* (number of gates used for estimating  $K_{DP}$ ) and *n\_iter* (number of re-estimations of  $K_{DP}$  per window). Higher values of these parameters result in smoother  $\Phi_{DP}$  profiles. Reimel and Kumjian (2021) found various parameter combinations worked well depending on precipitation complexity, leading us to test combinations from 2 to 14 for both parameters. Figure 6 shows multiple scatter plots comparing the performance of `kdp_vulpiani` for different values of *windsize* and *n\_iter* in estimating  $K_{DP}$ . The upper-  
 245 left corner panel shows the scatter of  $K_{DP}$  using the largest tested settings, whereas the lower-right corner panel shows the results for the smallest. Each row holds *windsize* constant while each column holds *n\_iter* constant. In the scatter plot for *windsize* = 14 and *n\_iter* = 14, the data is predominantly clustered under  $K_{DP}^{sc}$  for  $Z_H \geq 35$  dBZ, indicating underestima-



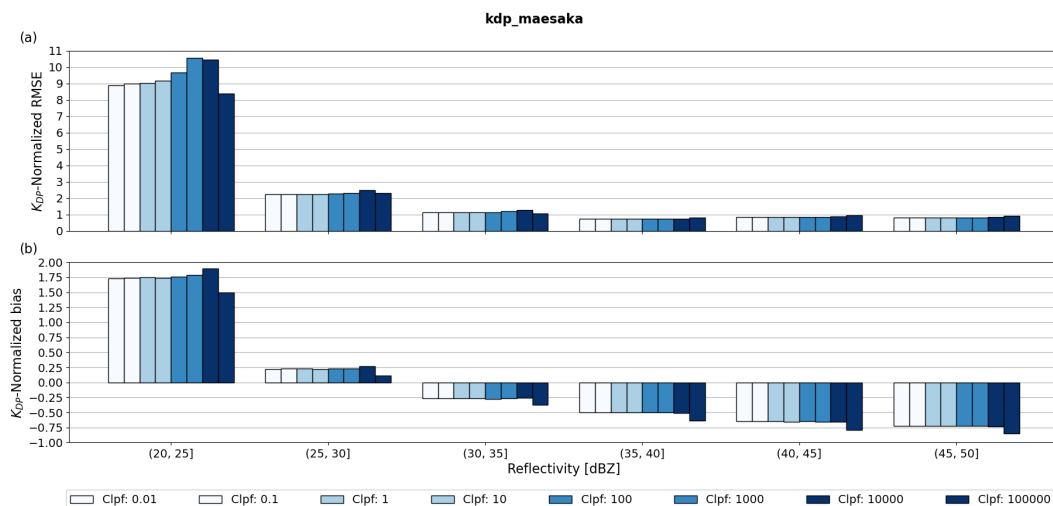


**Figure 5.** Panel (a) shows RMSE normalized by interval-averaged  $K_{DP}^{sc}$  of  $kdp\_maesaka$  relative to  $K_{DP}^{sc}$  as a function of reflectivity and for various values of  $Clpf$ ; panel (b) shows same as (a) but for the normalized bias metric.

tion of  $K_{DP}$ . For  $Z_H < 35$  dBZ, this parameter setting produces accurate and precise results. The results from the opposite extreme of Fig. 6 are slightly more accurate albeit significantly less precise; the scatter plot of  $windsize = 2$  and  $n\_iter = 2$  shows wider spread of  $K_{DP}$  data for all  $Z_H$  values, although with slightly enhanced clustering of data around  $K_{DP}^{sc}$  for  $Z_H \geq 35$  dBZ. These results indicate a trade-off between precision and accuracy when varying  $windsize$  and  $n\_iter$  from 14 to 2. Particularly, larger settings favoring precision while deteriorating accuracy, and smaller settings favoring accuracy with deteriorated precision.

To further analyse the trade-off between accuracy and precision when varying  $windsize$  and  $n\_iter$  in  $kdp\_vulpiani$ , Fig. 7(a)-(b) show the NRMSE and normalized bias of  $k_{DP}$  estimates with varying  $windsize$  and  $n\_iter$  as a function of  $Z_H$ . Figure 7(a) shows that  $windsize$  of 2 yielded the worst performance, implicating that the gain in accuracy by including fine-scale fluctuations in  $\Phi_{DP}$  is not enough to compensate the increased errors due to the inclusion of outliers. On the other hand,  $windsize$  of 14 shows good performance across the entire  $Z_H$  range. However, the predominantly negative normalized bias of  $windsize$  of 14 relative to smaller counterparts in Fig. 7(b) indicates that larger  $windsize$  leads to underestimation of  $K_{DP}$  more than lower  $windsize$  values. The consistent errors when varying  $n\_iter$  in Fig. 7(a) indicate that this parameter setting does not impact as strongly as  $windsize$  in the performance of  $kdp\_vulpiani$ , especially in low  $Z_H$ . However, results from Fig. 7(b) suggest that smaller  $n\_iter$  significantly reduces the underestimation of  $K_{DP}$  estimates when  $windsize$  is large. Our results strongly resemble those reported in Reimel and Kumjian (2021), indicating that smaller number of iterations and moderate window sizes significantly enhance the performance of  $kdp\_vulpiani$ . Particularly, among the RMSE heat maps of  $kdp\_vulpiani$  shown in Reimel and Kumjian (2021),  $windsize = 10$  and  $n\_iter = 2$  produced the best results, coinciding with the smallest 35-50-dBZ-averaged NRMSE in this study.



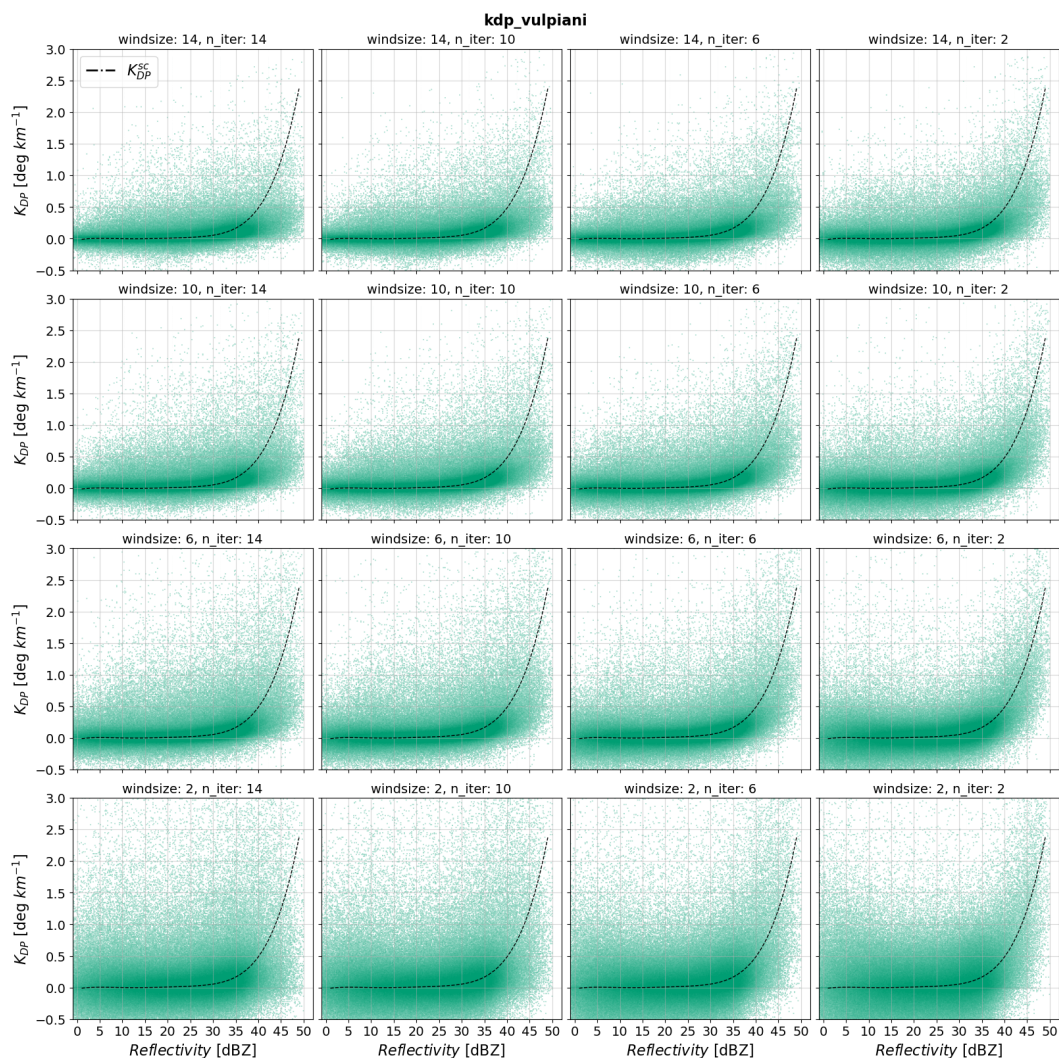


**Figure 6.** Scatter plots of estimated  $K_{DP}$  from `kdp_vulpiani` as function of reflectivity and for various values of  $windsize$  and  $n\_iter$ . Panels (a)–(p) show results with  $(windsize, n\_iter)$  tuples values from (14, 14) to (2, 2), decreasing  $windsize$  with increasing rows. The dashed black line corresponds to  $K_{DP}^{sc}$ .

### 3.1.3 PyArt’s Linear Programming method

270 PyArt’s implementation of an LP method proposed in Giangrande et al. (2013), `phase_proc_lp`, allows the user to tune the window length for smoothing  $\Phi_{DP}$ , `window_len`, and two intertwined parameters constraining the  $K_{DP}$  output via self-consistency relations: `self_const` and `coef`. The former is the weight of the self-consistency constraint and the latter is the exponent in the self-consistency relation linking  $K_{DP}$  to  $Z_H$ , given in Giangrande et al. (2013) as  $aZ_H^b$  but expressed in `phase_proc_lp` as  $(10^{0.1 \times Z_H})^{coef} / self\_const$ . Since information about the expected  $K_{DP}$  was known beforehand, given by  $K_{DP}^{sc}$ , we pro-

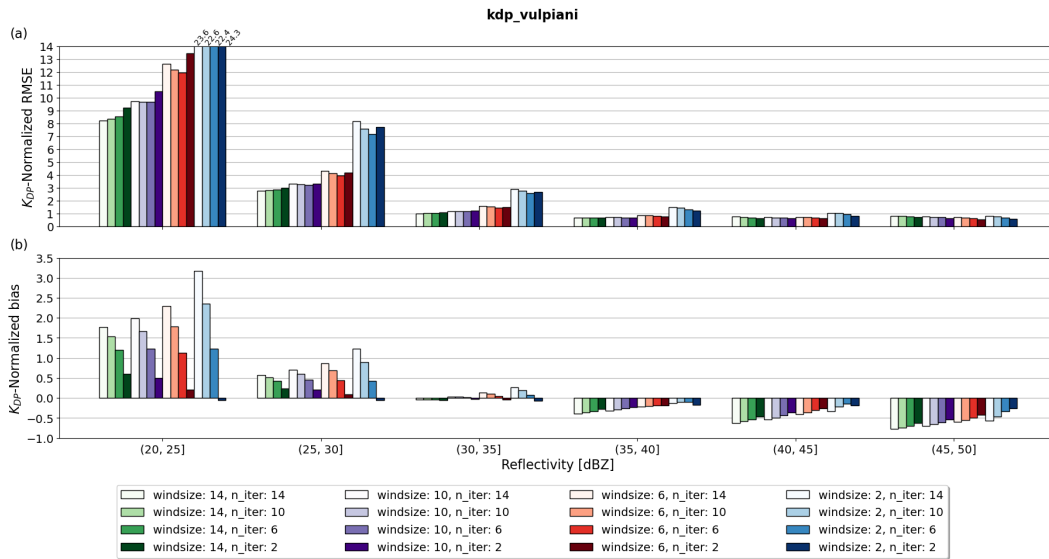


**Figure 7.** Panel (a) shows RMSE normalized by interval-averaged  $K_{DP}^{sc}$  of `kdp_vulpiani` relative to  $K_{DP}^{sc}$  as a function of reflectivity and for various values of `window_size` and `n_iter`; panel (b) shows same as (a) but for the normalized bias metric.

vided the method with the optimal values of  $self\_const = 10^4$  and  $coef = 0.914$ . In this way, the parameter optimization of  
 275 `phase_proc_lp` was focused solely on `window_len` variations.

The parameter `window_len` defines the window length for smoothing the LP-processed  $\Phi_{DP}$  field before  $K_{DP}$  is estimated. The default setting of this parameter is 35, indicating a smoothing window length of 17.5 km for a range resolution of 500 m. To include finer-scale precipitation features (e.g.  $\sim 2.5$  km), `phase_proc_lp` was tested with `window_len` values ranging from 5  
 280 to 40. Figure 8 shows multiple scatter plots comparing the performance of `phase_proc_lp` for different settings of `window_len` in estimating  $K_{DP}$ . Moving from the upper-left to the lower-right corner panels, Fig. 8 shows  $K_{DP}$  estimated using window lengths from 5 to 40 in intervals of 5. The scatter plot for `window_len = 5` shows data points predominantly clustered around  $K_{DP}^{sc}$  across the entire  $Z_H$  range, indicating strong correlation between  $K_{DP}$  and  $K_{DP}^{sc}$ . Even in high  $Z_H$  ranges (i.e.,  $\geq 35$  dBZ), the tight correlation between  $K_{DP}$  and  $K_{DP}^{sc}$  holds, indicating high accuracy and precision of  $K_{DP}$  in the presence of  
 285 heavy precipitation. The accuracy and precision of  $K_{DP}$  relative to  $K_{DP}^{sc}$  decreases progressively when `window_len` increases, indicated by the spreading and downward shifting of  $K_{DP}$  estimates relative to  $K_{DP}^{sc}$ . Especially for the range  $Z_H \geq 35$  dBZ, the scatter plots of `windows_len` from 25 to 40 show substantial underestimation of  $K_{DP}$  relative to  $K_{DP}^{sc}$ , indicating stronger oversmoothing of  $\Phi_{DP}$  for larger values of `window_len`. Comparing the scatter plots, `window_len = 5` undoubtedly shows the best performance of `phase_proc_lp`. This result agrees with `phase_proc_lp window_len` experiments by Li et al. (2023) in  
 290 an extreme heavy precipitation event, where small `window_len` yielded the best performance. Compared to the `phase_proc_lp` experiments by Reimel and Kumjian (2021), our results suggest that smaller `window_len` produce overall more accurate  $K_{DP}$

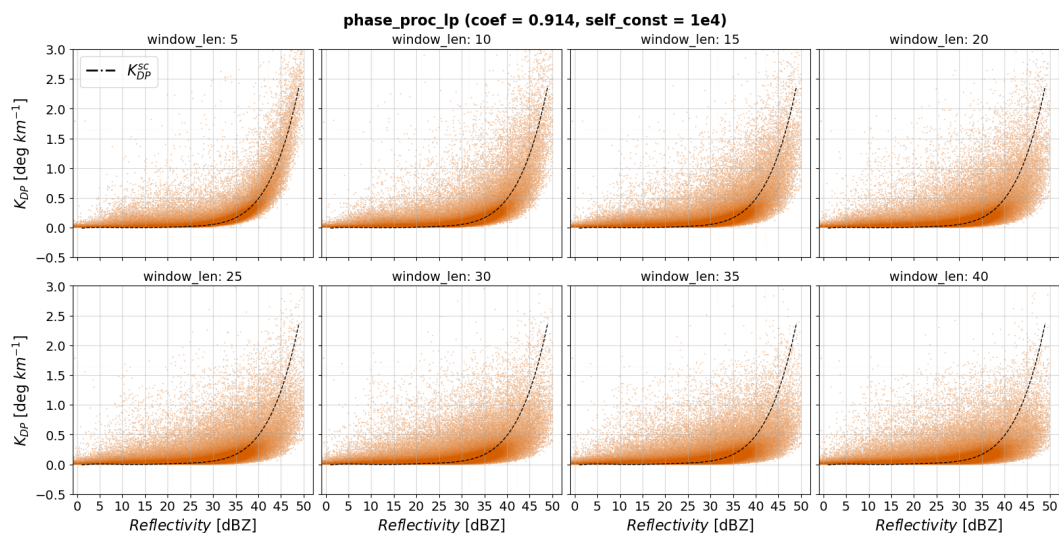


**Figure 8.** Scatter plots of estimated  $K_{DP}$  from `phase_proc_lp` as function of reflectivity and for various values of `window_len`. Panels (a)-(h) show results with `window_len` values from 5 to 40, while fixing `coef` to 0.914 and `self_const` to  $10^4$ . The dashed black line corresponds to  $K_{DP}^{sc}$ .

estimates. However, the influence of the self-consistency constraints proposed in Giangrande et al. (2013) plays a key role in this aspect; if optimal self-consistency constraints are not provided or do not match theoretical expectations, the precision and accuracy in  $K_{DP}$  significantly reduces and larger `window_len` values compensate this by oversmoothing  $\Phi_{DP}$  (see Appendix 295 A for results of the performance of `phase_proc_lp` with very little influence of self-consistency constraints).

To investigate further the effects of `window_len` in the performance of `phase_proc_lp`, Fig. 9(a)-(b) show the NRMSE and normalized bias of  $K_{DP}$  estimates with varying `window_len` as function of  $Z_H$ . In agreement with the patterns observed in the scatter plots from Fig. 8, `window_len` of 5 produced the best performance compared to other parameter settings. Interestingly, 300 even in light precipitation (e.g.  $Z_H < 30\text{dBZ}$ ) smaller values of `window_len` produced the best NRMSE metrics, indicating that larger `window_len` do not further improve the precision of `phase_proc_lp`. Instead, larger `window_len` enhanced the bias of  $K_{DP}$  relative to  $K_{DP}^{sc}$  as shown in Fig. 9(b). The parameter `window_len` of 5 produced undoubtedly the best metrics for `phase_proc_lp` and it was selected as the optimal parameter.

### 3.1.4 Wradlib's Vulpiani method

305 Wradlib's implementation of Vulpiani et al. (2012), `kdp_from_phidp`, features two optimizing parameters: `winlen` (number of gates used to reconstruct  $\Phi_{DP}$ ) and `dr` (gate length resolution in km). We tested `winlen` values from 3 to 11 and `dr` values from 0.5 to 4. Figure 10 shows multiple scatter plots of  $K_{DP}$  estimates using `kdp_from_phidp` varying settings of `winlen` and `dr`. Each row of scatter plots holds `winlen` constant while decreasing `dr` from left to right. Similarly, each column of scatter plots

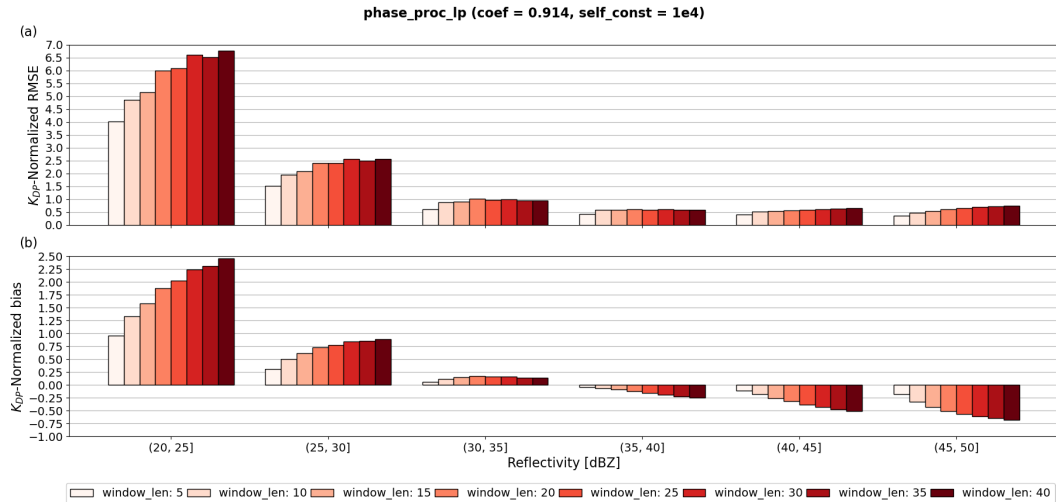


**Figure 9.** Panel (a) shows RMSE normalized by interval-averaged  $K_{DP}^{sc}$  of `phase_proc_lp` relative to  $K_{DP}^{sc}$  as a function of reflectivity and for various values of `window_len`; panel (b) shows same as (a) but for the normalized bias metric.

holds  $dr$  constant while decreasing  $winlen$  from top to bottom. The first scatter plot, i.e.,  $winlen = 11$  and  $dr = 4$ , shows  
 310  $K_{DP}$  clustered predominantly around  $0 \text{ deg km}^{-1}$  across the entire  $Z_H$  range, indicating substantial oversmoothing of  $\Phi_{DP}$ .  
 Even for  $Z_H \geq 30 \text{ dBZ}$ , the noticeable underestimation of  $K_{DP}$  relative to  $K_{DP}^{sc}$  indicates that `kdp_from_phidp` is not able to  
 capture signatures of heavy precipitation for large  $winlen$  and  $dr$  settings. Moving towards the right-most end of the first row  
 of scatter plots, a smaller  $dr$  enhances the accuracy of `kdp_from_phidp`, particularly for  $Z_H \geq 30 \text{ dBZ}$ . However, the gain in  
 accuracy comes together with loss in precision in  $K_{DP}$  estimates, indicated by the wider spread of data. In addition, decreasing  
 315  $dr$  makes `kdp_from_phidp` more prone to the inclusion of outliers, illustrated by data points with  $K_{DP} > 1 \text{ deg km}^{-1}$ , even  
 for  $Z_H \leq 20 \text{ dBZ}$ . The scatter plots from the second row follow the same behavior as in the first row except for wider spread  
 of data, suggesting that decreasing  $winlen$  while holding  $dr$  constant overall reduces the precision of `kdp_from_phidp`. When  
 moving from left to right in the second row of scatter plots, accuracy increases while precision decreases when decreasing  $dr$ .  
 In the last row,  $K_{DP}$  estimates are the most scattered for the same  $dr$ , indicating loss in precision of `kdp_from_phidp` when  
 320 reducing  $winlen$ . The scatter plot of  $K_{DP}$  for the smallest parameter settings tested ( $winlen = 3$  and  $dr = 0.5$ ) resembles a  
 scatter plot of random noise with no significant clustering of data, and suggesting extremely poor correlation relative to  $K_{DP}^{sc}$ .  
 Comparing the scatter plots row-wise and column-wise, decreasing  $winlen$  or  $dr$  significantly deteriorates the precision of  
 the method. However, the effect on the accuracy is more complex; simultaneous setting of  $winlen$  and  $dr$  to large values lead  
 to substantial underestimation of  $K_{DP}$ , whereas small values lead to noisy  $K_{DP}$ , respectively. These results suggest that the  
 325 effects of varying  $winlen$  and  $dr$  in the performance of `kdp_from_phidp` are strongly intertwined, requiring more analysis in  
 the trade-off between accuracy and precision offered by variations of these parameters.

To analyse the trade-off between accuracy and precision when  $winlen$  and  $dr$  in `kdp_from_phidp`, Fig. 11(a)-(b) show the





NRMSE and normalized bias of  $K_{DP}$  estimates with varying  $winlen$  and  $dr$  as function of  $Z_H$ . Even though Fig. 11(a) has  
330 been clipped at 5.0, it is important to notice the significantly high values when using the smallest  $dr$  (97.6, 135.4 and 278.6  
for  $winlen$  of 11, 7, and 3, respectively). The predominantly higher NRMSE values with the smallest  $dr$  indicate that the  
precision of  $kdp\_from\_phidp$  reduces significantly with  $dr < 1$  for any  $winlen$  tested. An exception occurs in the  $Z_H$  interval  
(45, 50] dBZ, where the smallest  $dr$  yield the best metrics due to slight improvements in the accuracy. Despite the limited  
amount of data within this  $Z_H$  interval (see Fig. 3), the clustering of  $K_{DP}$  around  $K_{DP}^{sc}$  in Fig. 10 and the small normalized  
335 biases in Fig. 11(b) suggest that accuracy improved slightly for the smallest  $dr$ . The smaller NRMSE with high  $dr$  in Fig.  
11(a) is counterbalanced by the predominantly larger negative bias for larger  $dr$  in Fig. 11(b). This implies that larger  $dr$  values  
in  $kdp\_from\_phidp$  lead to underestimation of  $K_{DP}$  for all  $winlen$  tested. As a conclusion, combining large  $winlen$  with  
smaller  $dr$  produces best performance in heavier precipitation (i.e.,  $Z_H > 30$  dBZ), whereas combining large  $winlen$  with  
larger  $dr$  produces best results for light precipitation. Overall, small values of  $winlen$  reduces significantly the precision in the  
340 method without improving accuracy. The parameter setting with the smallest 35-50-dBZ-averaged NRMSE was  $winlen = 11$   
and  $dr = 2$ .

### 3.2 Performance Assessment of methods Relative to $K_{DP}^{sc}$

With parameter-optimized  $kdp\_maesaka$ ,  $kdp\_vulpiani$ ,  $phase\_proc\_lp$  and  $kdp\_from\_phidp$ , and including  $kdp\_schneebeli$   
and  $kdp\_iris$ , we evaluated the relative performance of the methods by quantifying the uncertainties as a function of  $Z_H$ .  
345 To achieve this, a qualitative analysis with the use of  $K_{DP}$  vs.  $Z_H$  scatter plots for each method is provided in Sec. 3.2.1.  
These plots help to evaluate the relative performance of each method against benchmarking  $K_{DP}^{sc}$  as a function of  $Z_H$ . Then,  
a quantitative assessment of the method's performance is provided in Sec. 3.2.2, by quantifying the uncertainties associated to  
each method relative to  $K_{DP}^{sc}$  using the NRMSE and normalized bias metrics.

#### 3.2.1 Qualitative Assessment

350 We qualitatively assessed the precision and accuracy of the estimated  $K_{DP}$  using scatter plots of  $K_{DP}$  vs.  $Z_H$  for each method.  
Figure 12 shows six scatter plots comparing the performance of  $kdp\_maesaka$ ,  $kdp\_vulpiani$ ,  $phase\_proc\_lp$ ,  $kdp\_from\_phidp$ ,  
 $kdp\_schneebeli$  and  $kdp\_iris$  in estimating  $K_{DP}$ . Each scatter plot illustrate the relationship between estimated  $K_{DP}$  (y-axis)  
relative to  $Z_H$  (x-axis), against benchmarking  $K_{DP}^{sc}$  (black dashed line). For the parameter-optimized methods in Figs. 12(a)-  
(d), the optimal parameter selected is indicated in the plot's title together with the method's name. Comparing the scatter  
355 plots,  $phase\_proc\_lp$  demonstrates the highest accuracy and precision, evidenced by the data narrowly clustered around  $K_{DP}^{sc}$   
across the entire  $Z_H$  range. Methods  $kdp\_from\_phidp$  and  $kdp\_schneebeli$  show the least accuracy and precision, with broader  
spread and more outliers, particularly when  $Z_H < 30$  dBZ. For higher  $Z_H$  values, even though  $kdp\_from\_phidp$  shows better  
precision but worse accuracy than  $kdp\_schneebeli$ , these two methods strongly underestimate  $K_{DP}$ , evidenced by the pre-  
dominant clustering of  $K_{DP}$  estimates below  $0.5 \text{ deg km}^{-1}$ . Method  $kdp\_maesaka$  shows less scattering of  $K_{DP}$  estimates  
360 compared to  $kdp\_from\_phidp$  and  $kdp\_schneebeli$ , indicating higher precision and accuracy particularly for  $Z_H < 30$  dBZ.  
However, for  $Z_H \geq 30$  dBZ, the performance of  $kdp\_maesaka$  deteriorates rapidly, as shown by the broader spread and sig-

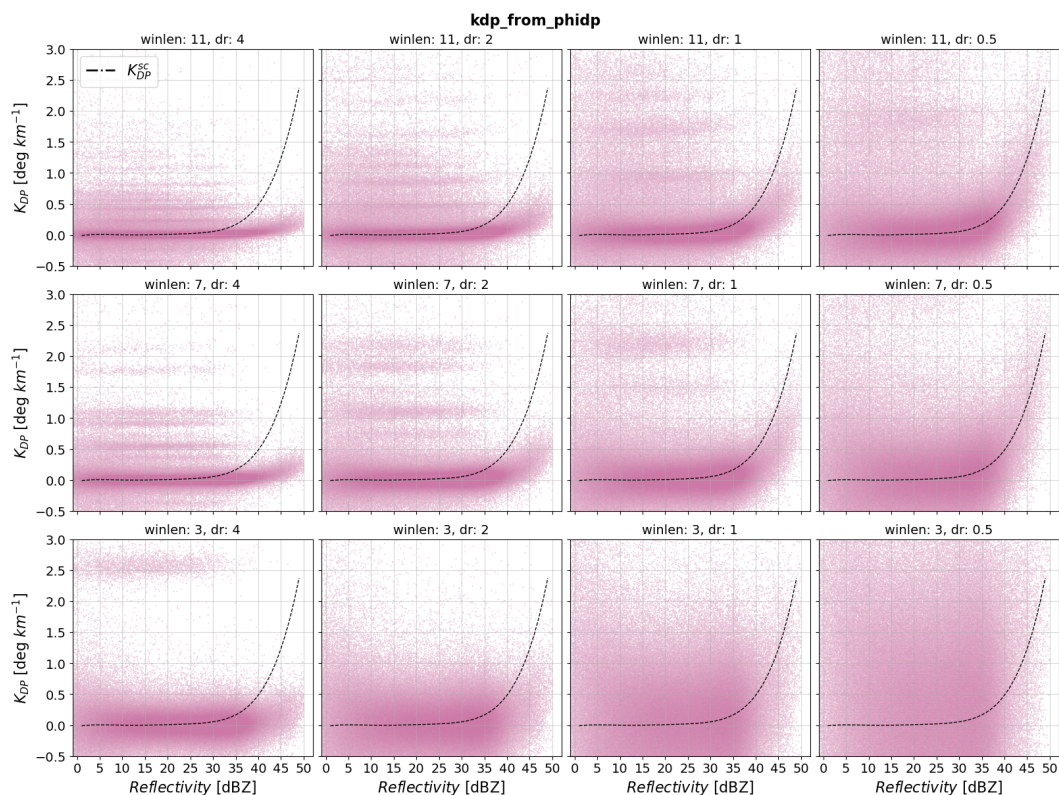


**Figure 10.** Scatter plots of estimated  $K_{DP}$  from `kdp_from_phidp` as function of reflectivity and for various values of  $winlen$  and  $dr$ . Panels (a)–(l) show results with  $(winlen, dr)$  tuples values from (11, 4) to (3, 0.5);  $winlen$  decreases in intervals of 4 per row whereas  $dr$  decreases by half per column. The dashed black line corresponds to  $K_{DP}^{sc}$ .

nificant underestimation of  $K_{DP}$  relative to  $K_{DP}^{sc}$ . Methods `kdp_vulpiani` and `kdp_iris` show moderate performance, with better accuracy and precision than `kdp_from_phidp`, `kdp_schneebeli` and `kdp_maesaka`, but less than `phase_proc_lp`. Between methods `kdp_vulpiani` and `kdp_iris`, `kdp_vulpiani` shows better correlation of  $K_{DP}$  estimates with  $K_{DP}^{sc}$  for  $Z_H \geq 35$  dBZ, indicating higher accuracy in heavier precipitation. However, `kdp_iris` shows less scattering across the entire  $Z_H$  range, indicating overall higher precision than `kdp_vulpiani`. Methods `kdp_vulpiani`, `kdp_from_phidp`, `kdp_schneebeli` and `kdp_iris` include negative  $K_{DP}$  values, which should not be expected in rain observations. These negative estimates show up predominantly in lighter precipitation (i.e.,  $Z_H < 30$  dBZ), indicating they are most likely produced by noise in  $\Phi_{DP}$ . However, the inclusion of negative  $K_{DP}$  estimates are useful, for instance, in the detection of snow crystals, allowing `kdp_vulpiani`, `kdp_from_phidp`, `kdp_schneebeli` and `kdp_iris` to be used in a wider range of applications when compared to `kdp_maesaka` and `phase_proc_lp`. The relatively high accuracy and precision of `kdp_iris` and `kdp_vulpiani`, together with the inclusion of negative  $K_{DP}$  estimates, leave these two methods as well-suited candidates for QPE, calibration and hydrometeor classification routines.

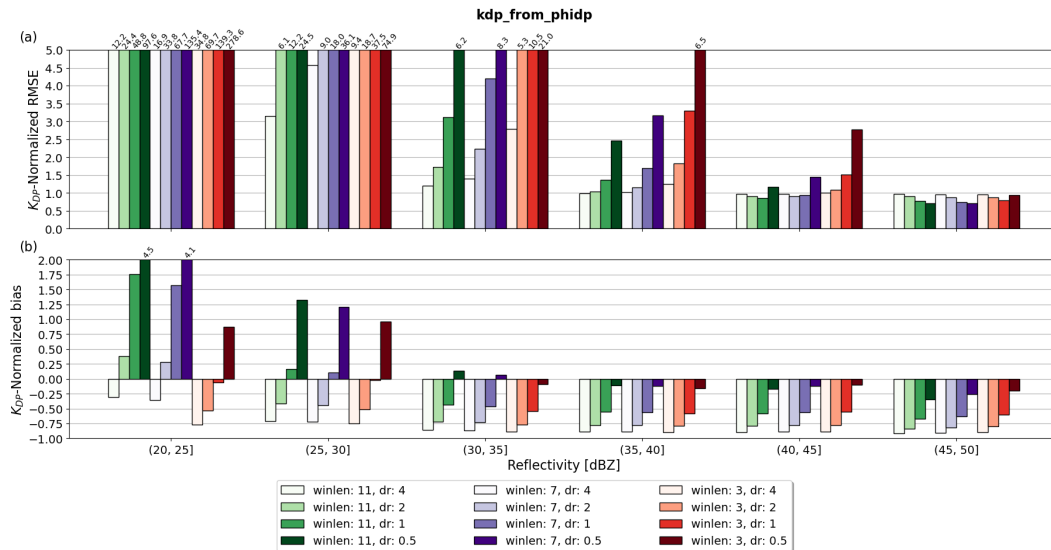


**Figure 11.** Panel (a) shows RMSE normalized by interval-averaged  $K_{DP}^{sc}$  of  $kdp\_from\_phidp$  relative to  $K_{DP}^{sc}$  as a function of reflectivity and for various values of  $winlen$  and  $dr$ ; panel (b) shows same as (a) but for the normalized bias metric. The numbers on top of the bars indicate the values of the metric exceeding the y-axis limit selected

### 3.2.2 Quantitative Assessment

The quantitative assessment of the methods was achieved throughout the metrics NRMSE and normalized bias, and complemented with statistics from the Wasserstein distance (WD) (Ramdas et al., 2015). The WD measures the similarity between two cumulative distributions, given in this study by  $K_{DP}$  estimated by each method, and  $K_{DP}^{sc}$ . On the one hand, NRMSE and normalized bias computed as a function of  $Z_H$ , allows the assessment of relative accuracy and precision of the methods based on precipitation intensities. The WD, on the other hand, estimated independently from each radar scan and with statistics over the entire set of scans, allows the assessment of the relative consistency and robustness of the methods.

380

Figures 13(a)-(b) show NRMSE and normalized bias of estimated  $K_{DP}$  for each method. Overall,  $phase\_proc\_lp$  shows the best performance, as evidenced by the lowest NRMSE values in Fig. 13(a) and moderately low bias in Fig. 13(b) across all  $Z_H$  intervals. In contrast,  $kdp\_schneebeli$  shows the worst performance among the methods, indicated by the highest NRMSE values and moderately high bias across all  $Z_H$  intervals. Method  $kdp\_from\_phidp$  shows substantially higher NRMSE values than  $kdp\_maesaka$ ,  $kdp\_vulpiani$ ,  $phase\_proc\_lp$  and  $kdp\_iris$  but significantly smaller than  $kdp\_schneebeli$ , particularly for the smallest  $Z_H$  values. The relatively small bias of  $kdp\_from\_phidp$  when NRMSE values are substantially high, is explained by the positive-to-negative symmetrical spread of  $K_{DP}$  estimates around the x-axis, indicating poor precision. Additionally, the persistent negative and large normalized bias of this method relative to the other methods indicates  $kdp\_from\_phidp$  underestimates  $K_{DP}$  the most. Methods  $kdp\_maesaka$ ,  $kdp\_vulpiani$  and  $kdp\_iris$  have moderate NRMSE values, performing

385



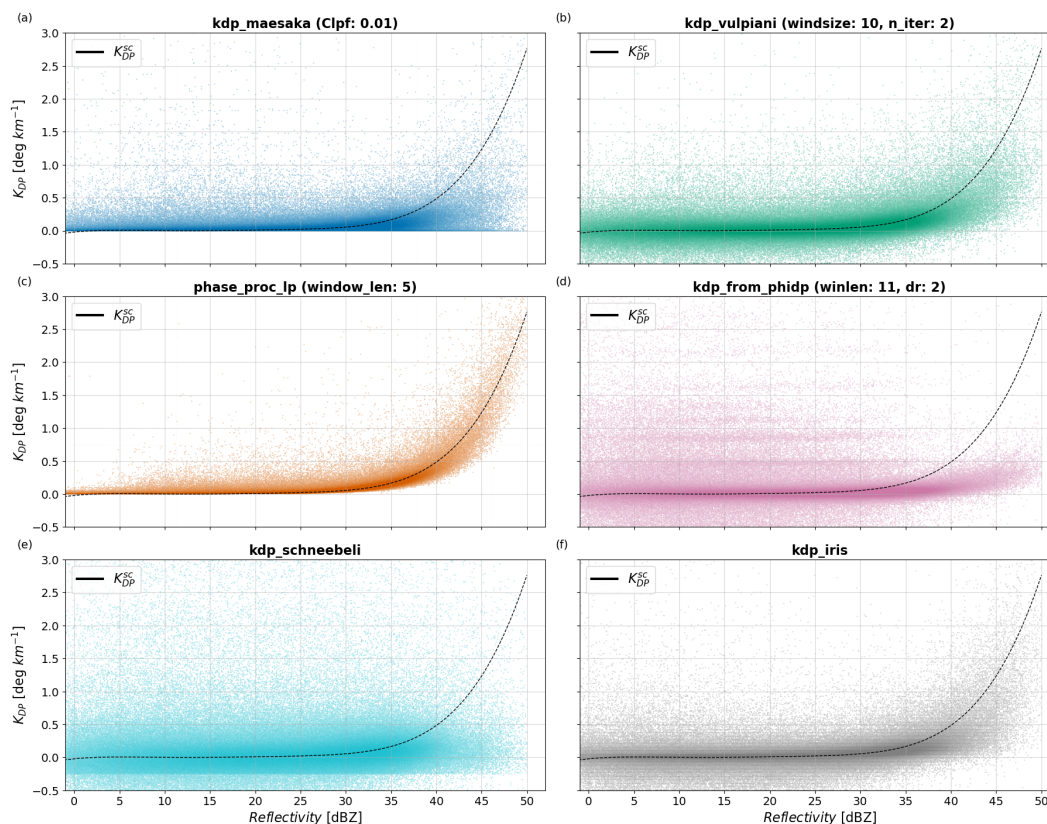


**Figure 12.** Scatter plot of estimated  $K_{DP}$  from each parameter-optimized method relative to  $K_{DP}^{sc}$  as function of reflectivity. Panels (a)–(f) show *kdp\_maesaka*, *kdp\_vulpiani*, *kdp\_iris*, *phase\_proc\_lp*, *kdp\_from\_phi\_dp* and *kdp\_schneebeli*, respectively. The dashed black line corresponds to  $K_{DP}^{sc}$ .

390 better than *kdp\_schneebeli* and *kdp\_from\_phidp* but not as well as *phase\_proc\_lp*. Among these three methods, *kdp\_maesaka* has the smallest NRMSE values for  $Z_H \leq 35$  dBZ but the largest when  $Z_H \geq 40$  dBZ. The relatively large positive bias of *kdp\_maesaka* when  $Z_H < 30$  is a direct consequence of the exclusion of negative  $K_{DP}$  estimates. However, the persistent larger negative bias of *kdp\_maesaka* relative to *kdp\_vulpiani* and *kdp\_iris* when  $Z_H \geq 30$  dBZ, indicates stronger underestimation of  $K_{DP}$  and thus lesser accuracy. These results indicate that, in comparison to others, *kdp\_maesaka* performs slightly  
 395 better in light precipitation (i.e.,  $Z_H < 30$  dBZ) but worse in heavier precipitation. Between *kdp\_vulpiani* and *kdp\_iris*, *kdp\_iris* shows overall smaller NRMSE and normalized bias, indicating higher accuracy and precision than *kdp\_vulpiani*.

Complementary to NRMSE and normalized bias metrics, we evaluated the consistency and robustness of the methods using the Wasserstein distance (WD). The WD was computed for each radar scan independently using the *wasserstein\_distance* module from SciPy (Virtanen et al., 2020). Then, the statistics from the estimated WD values for all scans were visualized  
 400 and analysed using using boxplots. Figure 14 consists of two panels comparing the WD boxplots of the methods. Figure 14(a) compares the WD for all methods, including *kdp\_schneebeli*, which presented significantly large WD. Figure 14(b) presents

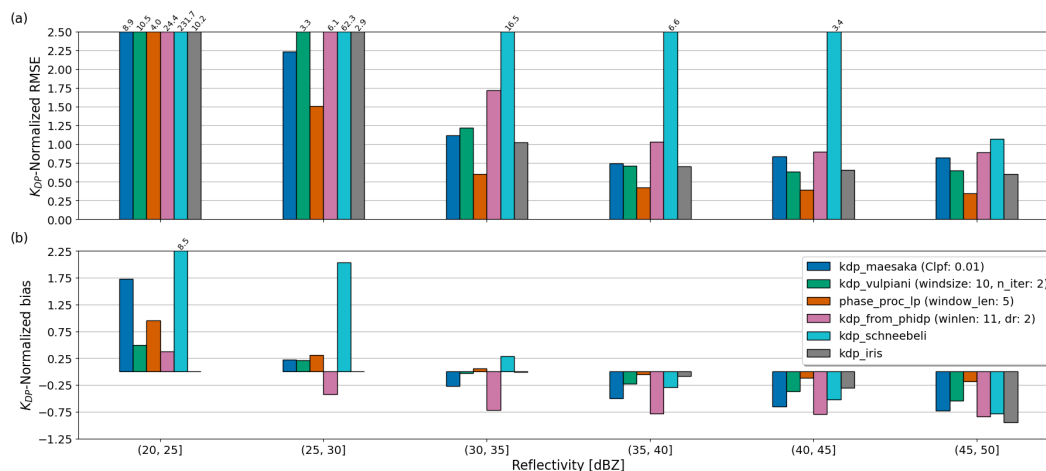


**Figure 13.** Panel (a) shows bias of estimated  $K_{DP}$  from each parameter-optimized method relative to  $K_{DP}^{SC}$  as function of reflectivity; panel (b) shows same as (a) but bias normalized by interval-averaged  $K_{DP}^{SC}$ . The numbers on top of the bars indicate the values of the metric exceeding the y-axis limit selected

the same data as (a) but excluding `kdp_schneebeli` to better compare the remaining methods. Each boxplot summarizes the statistics of estimated WD by showing the median (black dashed line), interquartile ranges (IQR),  $1.5 \times$  the IQR (whiskers) and outliers (crosses). The insights provided by boxplots in this analysis are twofold. First, a WD median closer to 0 indicates higher similarity between the cumulative distributions of a method’s estimated  $K_{DP}$  and that from  $K_{DP}^{SC}$ , ultimately indicating higher accuracy. Second, a narrower IQR indicates less variability of a method’s performance between scans, indicating higher consistency.

In Figure 14(a), the x-axis lists six methods: `kdp_maesaka`, `kdp_vulpiani`, `phase_proc_lp`, `kdp_from_phidp`, `kdp_schneebeli` and `kdp_iris`. The y-axis measures the WD values, ranging from 0 to 2. The boxplot for method `kdp_schneebeli` shows the largest WD with a median of 0.33, an IQR from 0.18 to 0.45, and several outliers. The other methods (`kdp_maesaka`, `kdp_vulpiani`, `phase_proc_lp`, `kdp_from_phidp` and `kdp_iris`) have median WD values ranging from 0.0 to 0.1, with smaller IQRs and fewer outliers. In Figure 14(b), method `kdp_schneebeli` is excluded, allowing for a clearer comparison of methods `kdp_maesaka`, `kdp_vulpiani`, `phase_proc_lp`, `kdp_from_phidp` and `kdp_iris`. The y-axis is rescaled to range from 0.0 to 0.2 for better visualization. Method `phase_proc_lp` has the lowest WD median at 0.01 with a narrow IQR from 0.008 to 0.018. Method `kdp_from_phidp` has significantly larger WD median of 0.098 and IQR from 0.077 to 0.122. Methods `kdp_maesaka` and `kdp_iris` have WD medians of 0.026 and 0.041, respectively, with moderate IQR and few outliers. Method `kdp_vulpiani` has a moderate WD median of 0.049 but noticeably wider IQR from 0.033 to 0.096 when compared to `kdp_maesaka`, `phase_proc_lp`, `kdp_from_phidp` and `kdp_iris`.

420



The large WD median of `kdp_schneebeli` indicates it performs worse compared to the other methods, overshadowing the performance difference among the remaining methods. Additionally, the large IQR of `kdp_schneebeli` implies that the method does not perform consistently thus reducing its reliability. Method `phase_proc_lp` demonstrates the best and consistent performance with the lowest WD median and narrowest IQR. These results additionally indicate that the distribution of  $K_{DP}$  estimated from `phase_proc_lp` is the closest to  $K_{DP}^{sc}$ . It is important to remember here that `phase_proc_lp` is supported by self-consistency relations constraining  $K_{DP}$  estimates based on  $Z_H$  observations, ultimately enhancing its accuracy and stability. The moderate IQR and significantly larger WD median of `kdp_from_phidp`, indicate its performance is consistent albeit less accurate relative to the other methods. Method `kdp_vulpiani` in turn, has a moderate WD median but relatively larger IQR, indicating better accuracy than `kdp_from_phidp` although less consistent. Methods `kdp_maesaka` and `kdp_iris` show similar consistency and accuracy, evidenced by their relatively low WD medians and moderate IQRs. These findings suggest that while `kdp_schneebeli` is the less accurate and consistent, the performance among the remaining methods vary, with `phase_proc_lp` presenting the highest robustness provided the method with quality-controlled  $Z_H$  and optimized self-consistency settings.

### 3.3 Consistency Analysis of $K_{DP}$ Retrievals from methods

Each method has its unique combination of mathematical approach, data requirements, and constraints (see Table 1), indicating uniqueness in the  $K_{DP}$  fields produced. How similar or dissimilar are these outputs is not clearly visible from the metrics computed nor the scatter plots displayed in Sec. 3.2. To answer this question, we study the consistency among methods using  $K_{DP}$  vs  $K_{DP}$  correlation plots shown in Fig. 15. Each scatter plot in Fig. 15 shows the relationship between  $K_{DP}$  estimated by a method (y-axis) with respect to  $K_{DP}$  estimated from a different method (x-axis) and the Pearson correlation coefficient ( $R$ ) is shown in the upper left corner of each scatter plot. The axes range from  $-0.5$  to  $3.0 \text{ deg km}^{-1}$  to include negative  $K_{DP}$  estimates. This part of the analysis does not require any ground-truth framework, allowing the use the entirety of radar dataset, i.e., including the attenuated observations (see red data in Fig. 3).

In Figure 15, the scatter plot of `kdp_iris` against `kdp_vulpiani` shows the best correlation among the methods, illustrated by the data significantly clustered along the diagonal and corroborated by the highest  $R$  of 0.66. Methods `kdp_iris` and `kdp_vulpiani` correlate similarly to `phase_proc_lp`, indicated by the second highest  $R$  of 0.65 for both. In relation to `kdp_maesaka`, the consistencies of `kdp_iris` and `kdp_vulpiani` are rather moderate, whereas in relation to `kdp_from_phidp` and `kdp_schneebeli`, they are significantly poorer. Among the methods, `kdp_schneebeli` correlates the least with any of the methods, evidenced by the data widely spread along the axes and showing negligible clustering of data along the diagonal. Particularly `kdp_schneebeli` against `kdp_from_phidp` shows the worst consistency with  $R = 0$  and the majority of data clustered around the x- and y-axis. Method `phase_proc_lp` correlates moderately to `kdp_maesaka` with an  $R = 0.41$ , although the scatter plot does not exhibit any particular pattern or clustering of data along the diagonal. Relative to `kdp_from_phidp`, `phase_proc_lp` shows significantly lower  $R$  despite the clear data correlation off of the diagonal. However, the small  $R$  value becomes evident when observing the dense clustering of data around  $0 \text{ deg km}^{-1}$  for `phase_proc_lp`. This results indicates the consistency between `kdp_from_phidp` and `phase_proc_lp` is highly influenced by the negative  $K_{DP}$  estimates in `kdp_from_phidp` that are mapped to  $0 \text{ deg km}^{-1}$  in

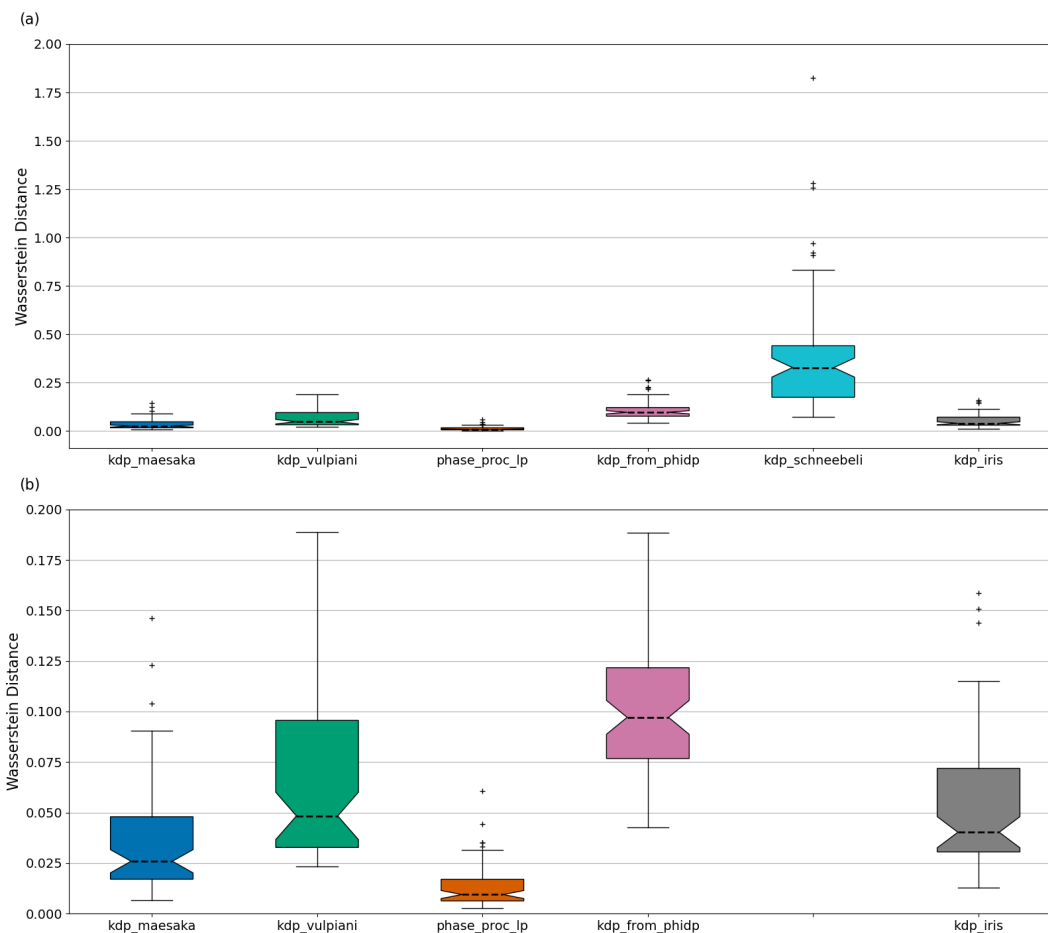


**Figure 14.** Panel (a) shows the boxplot of computed WD for each parameter-optimized method; panel (b) shows same as (a) but excluding kdp\_schneebeli for better visualization of the outperforming methods. The boxplot displays the WD median (black dashed line), IQRs (boundaries of the box),  $1.5 \times$  the IQR (whiskers) and the outliers (black crosses).

455 phase\_proc\_lp. Overall, the scatter plots show that kdp\_from\_phidp underestimates  $K_{DP}$  relative to the other methods. Method kdp\_maesaka shows no significant correlation with any method, with the largest  $R$  being 0.41 relative to both phase\_proc\_lp and kdp\_vulpiani.

## 4 Conclusions

In this study, we conducted a comprehensive evaluation of several  $K_{DP}$  estimation methods using C-band weather radar data, with a focus on their performance in rainfall observations. We employed a self-consistency framework, that links  $Z_H$  and  $Z_{dr}$  observations with  $K_{DP}$ , as the basis for our evaluations. This approach allows for the construction of the reference  $K_{DP}$  observations that can be used to assess the accuracy and robustness of the studied  $K_{DP}$  estimation methods. The use of the

460

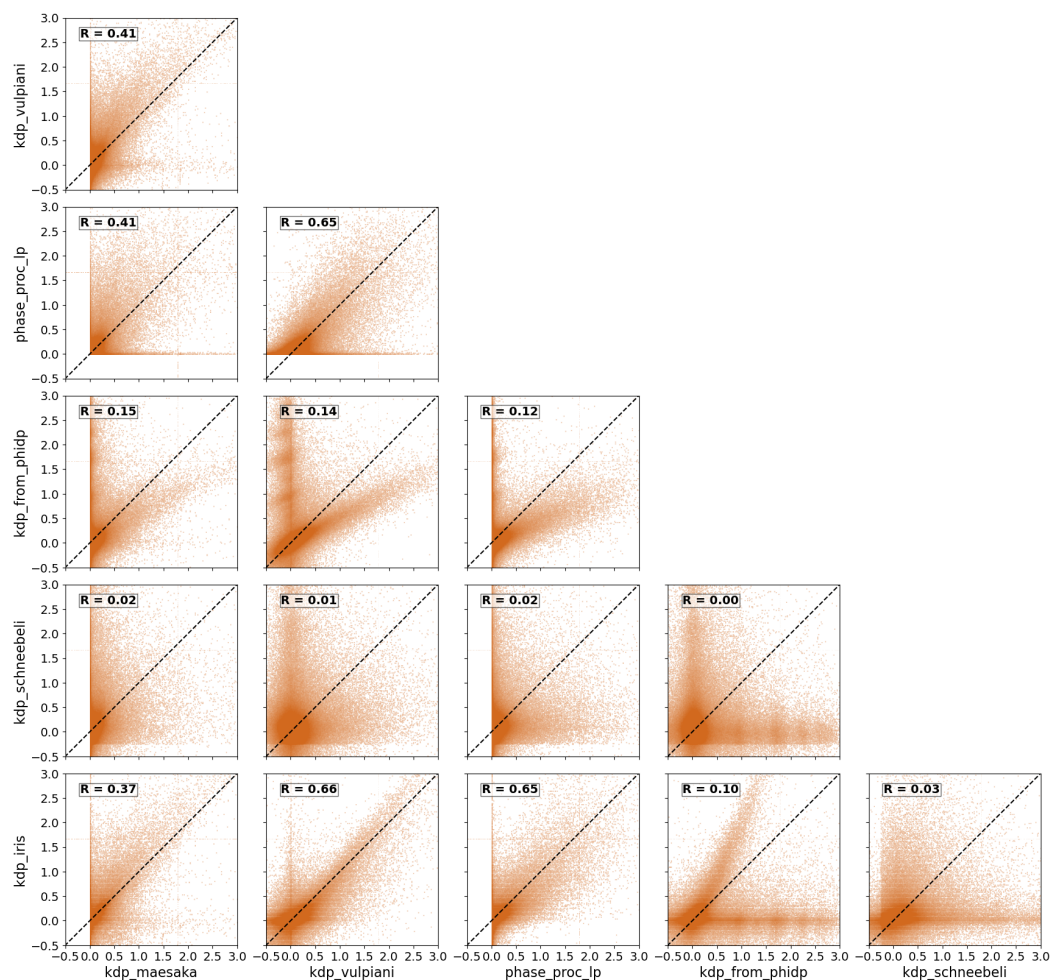


**Figure 15.** Correlation plot between the methods. Each scatter plot shows the relationship between two different methods without repetition and no method is compared to itself. The x- and y-axis represent  $K_{DP}$  estimated by a method in units of  $\text{deg km}^{-1}$ . Each plot shows the Pearson correlation coefficient between the two compared methods.

self-consistency framework requires rather strict quality control which is described in the paper.

465 Some, four out of six, of the  $K_{DP}$  estimation methods have user-configurable parameters. Using the proposed evaluation framework we could define optimized parameter settings. Most of the methods showed significant improvement in the performance after the optimization.

470 By comparing the relative performances of the estimation methods over the range of rain intensities, as characterized by the radar  $Z_H$  values, we have found significant difference in performances of the evaluated methods. Overall, implementations



of Giangrande et al. (2013), Vulpiani et al. (2012) and Wang and Chandrasekar (2009) exhibited the lowest NRMSE and normalized biases over the studied range, from 20 to 50 dBZ of  $Z_H$  values.

Our comparative analysis revealed that while the implementation of Giangrande et al. (2013)'s method stands out for its high accuracy and precision, its performance is heavily dependent on the provided self-consistency constraint. Without proper optimization of the self-consistency relation, linking  $Z_H$  and  $K_{DP}$ , and quality control of  $Z_H$ , even the best window length setting for this method can lead to suboptimal results, i.e. higher RMSE and  $K_{DP}$  underestimation at higher  $Z_H$  values. It should be noted, however, since the reference framework and Giangrande et al. (2013)'s method both use consistency relations  $K_{DP}(Z_H Z_{dr})$  and  $K_{DP}(Z_H)$ , respectively, they are not independent. Therefore, it is possible that the part of reported performance is caused by this dependence. Implementations of Vulpiani et al. (2012) and Wang and Chandrasekar (2009) showed good performance and do not require use of other radar variables, which potentially make them less sensitive to radar data quality issues, such as calibration and attenuation.

An additional qualitative comparison of the methods performances was carried out by computing correlations of derived  $K_{DP}$  values from the dataset that also included attenuated radar observations. The correlation between  $K_{DP}$  values estimated using different methods is not very high. The highest correlation values of 0.65-0.66 were observed between Giangrande et al. (2013), Vulpiani et al. (2012) and Wang and Chandrasekar (2009) methods. This indicates that uncertainty between different precipitation estimates could stem from the differences in the used  $K_{DP}$  methods.

The study is based on the self-consistency framework that limits it to the cases where no significant attenuation is observed. Additionally, the scope of our study is limited to the Finnish climatology and a single radar frequency, namely C-band radar observations. Despite these limitations, our findings offer valuable guidance for the use of  $K_{DP}$  estimation methods in rainfall observations. These results have significant implications for both operational radar network and hydrometeorological research, where the accuracy, precision, and stability of  $K_{DP}$  estimates are crucial.

#### 495 **Appendix A: Influence of self-consistency constraint in *phase\_proc\_lp***

Figure A1 shows same scatter plots as in 8, with  $K_{DP}$  estimated from *phase\_proc\_lp* using *self\_const* of  $10^6$  instead of  $10^4$ . The motivation behind was to study the performance of *phase\_proc\_lp* with little influence of self-consistency constraints. In Giangrande et al. (2013), the non-negativity condition in  $K_{DP}$  estimates is ensured by restricting the b-vectors:  $\mathbf{b} \geq 0$ . In addition, to produce more realistic  $K_{DP}$  estimates, they introduced the self-consistency relation  $K_{DP}(Z_H) = aZ_H^b$  to bound the estimates based on observed  $Z_H$ , requiring that the user provides quality controlled data. The restriction of the b-vectors becomes  $\mathbf{b} \geq aZ_H^b$ , which in *phase\_proc\_lp* is implemented as  $\mathbf{b} \geq (10^{0.1 \times Z_H})^{coef} / self\_const$ . Therefore, a two order of magnitudes larger *self\_const* value was used in this study to test the performance of *phase\_proc\_lp* with a significantly reduced influence of self-consistency constraints. The scatter plots show  $K_{DP}$  data clustered around  $K_{DP}^{sc}$  up to 35 dBZ. Beyond



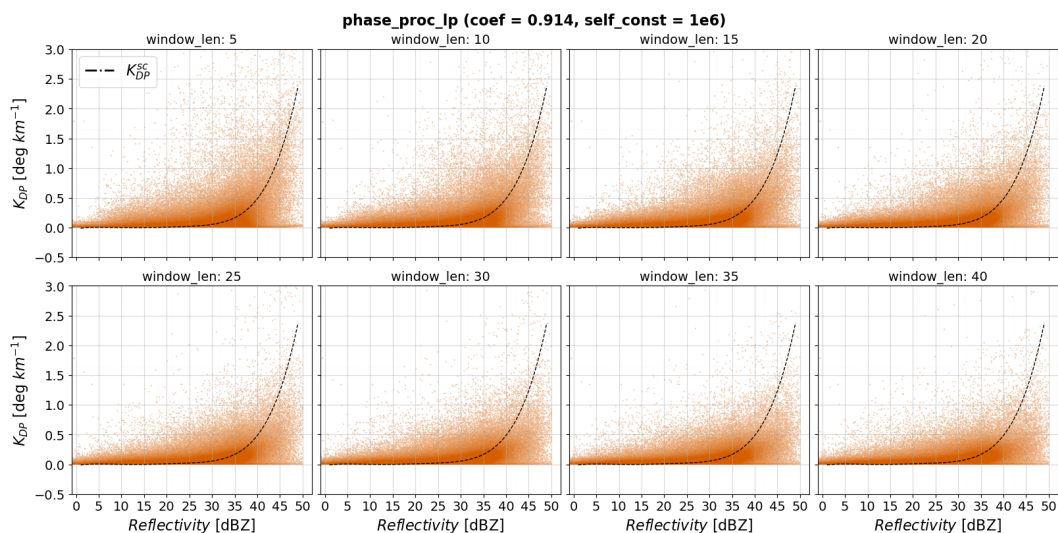


**Figure A1.** Scatter plots of estimated  $K_{DP}$  from `phase_proc_lp` as function of reflectivity and for various values of `window_len`. Panels (a)-(h) show results with `window_len` values from 5 to 40, while fixing `coef` to 0.914 and `self_const` to  $10^6$ . The solid black line denotes corresponds to  $K_{DP}^{sc}$ .

this threshold, precision and accuracy decays significantly regardless of the window length. However, in scatter plots with larger window lengths  $K_{DP}$  data is less scattered across the entire  $Z_H$  range and only slightly less accurate after 35 dBZ.

To further investigate the effects of the self-consistency constraint in `phase_proc_lp`, Fig. A2(a)-(b) show the normalized RMSE and bias of  $K_{DP}$  (estimated with `self_const` =  $10^6$ ) relative to  $K_{DP}^{sc}$ . Interestingly, the normalized RMSE in Fig. A2(a) behaves inversely as in normalized RMSE in Fig. 9, whereas normalized bias shows similar behavior for both. The opposite behaviors in normalized RMSE results indicate that window length has a strong impact in the performance of `phase_proc_lp` depending on whether the adequate self-consistency settings were provided; if so, smaller window lengths yield better performance by capturing fine scale precipitation features specially in heavy precipitation. In the opposite case, larger window lengths yield better performance by oversmoothing  $\Phi_{DP}$  thus reducing the impact of noise at the expense of losing fine-scale precipitation features. The oversmoothing effect from larger window lengths in  $K_{DP}$  is also implied from the normalized bias shown in Fig. A2(b); larger window lengths produced absolute largest biases in both extremes of the  $Z_H$  range. In addition, even though the normalized bias shows similar behavior for `self_const` =  $10^6$  and `self_const` =  $10^4$ , the latter produces larger differences between window lengths, indicating that high accuracy and precision of `phase_proc_lp` predominates in smaller window lengths, provided the adequate self-consistency constraints and quality-controlled  $Z_H$ .



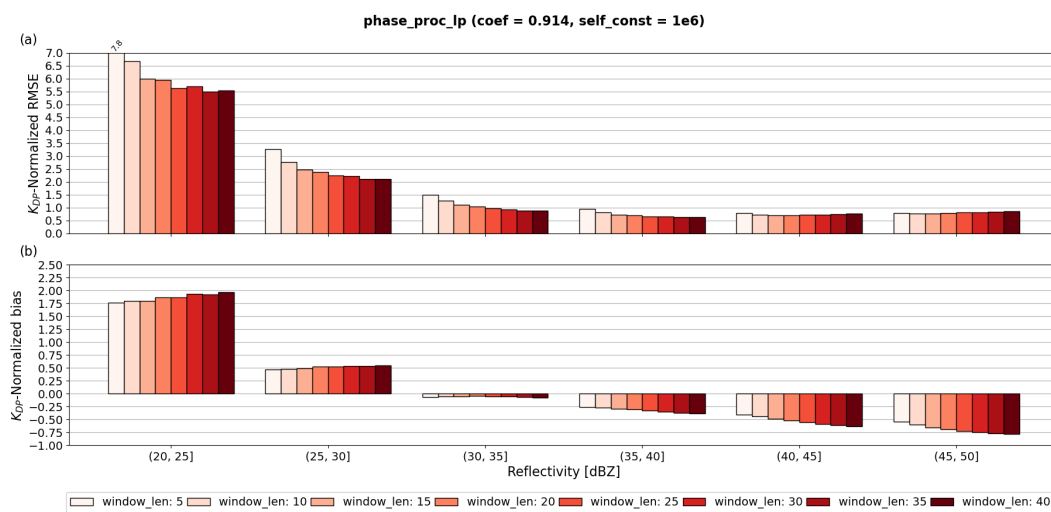


**Figure A2.** Panel (a) shows RMSE normalized by interval-averaged  $K_{DP}^{sc}$  of phase\_proc\_lp relative to  $K_{DP}^{sc}$  as a function of reflectivity and for various values of *window\_len*; panel (b) shows same as (a) but for the normalized bias metric.



## Data Availability

520 The radar raw data and KDP dataset, accessed via the link in Aldana (2024), includes the raw radar data and KDP processed data used to analyse the KDP estimation methods. The data has been processed using Python and it includes:

- The folder "radar" includes several subfolders: "yyyy/mm/dd/iris/raw/VAN". The "VAN" subfolder includes the .raw radar with PPI's observed by Vantaa radar at an elevation angle of 0.7 for a specific time: "yyyymmddHHMM\_VAN.PPI3\_B.raw". This data can be further read with PyArt (Helmus and Collis, 2016).

525 – The folder "KDP\_data" includes 5 .hdf5 files storing tables containing information about date (in pandas numerical value. It requires transformation to datetime object), Z (in dBZ), Zdr (in dB), attenuated gate (as boolean), theoretical or self-consistency KDP (in deg / km) and computed KDP (in deg / km) from a given method for different settings. The method is indicated in the name of the file as kdp\_method\_scatter.hdf5, where method can be:

- 'iris\_sch', referring to table containing KDP from iris software (used in the Finnish Meteorological Institute) and KDP computed from PyArt's implementation of Schneebeli et al. (2014). These two methods were computed together because only one KDP output was retrieved. They do not feature any user-configurable parameters to test.
- 'mae', referring to table containing KDP computed from PyArt's implementation of Maesaka et al. (2012). The columns correspond to KDP computed by varying parameter 'Clpf'.
- 'vulpiani', referring to table containing KDP computed from PyArt's implementation of Vulpiani et al. (2012). The columns correspond to KDP computed by varying parameters 'windsize' and 'n\_iter'.
- 'pplp', referring to table containing KDP computed from PyArt's implementation of Giangrande et al. (2013). The columns correspond to KDP computed by varying parameter 'windowlen'.
- 'wradlib', referring to table containing KDP computed from Wradlib's implementation of Vulpiani et al. (2012). The columns correspond to KDP computed by varying parameters 'winlen' and 'dr'.

540 The disdrometer dataset to obtain the DSD parameters and be accessed via the link provided in Moisseev (2024).

## Author Contributions

MA conducted the investigation process, collected the data, performed the formal analysis of the data and visualization; MA, SP and DM designed the methodology; SP, AL, MK and DM formulated the research goals and aims; AL and DM provided data; MA prepared the manuscript draft; MA, SP, AL, MK and DM reviewed, commented and edited the manuscript.

## 545 Competing Interests

The contact author has declared that none of the authors has any competing interests



## Acknowledgements

We thank Jenna Ritvanen for her valuable comments for improving the visualization of the data; we thank colleagues from the Early Career Community at the Finnish Meteorological Institute for feedback on how to make the manuscript reachable also  
550 for general audience.



## References

- Al-Sakka, H., Boumahmoud, A.-A., Fradon, B., Frasier, S. J., and Tabary, P.: A New Fuzzy Logic Hydrometeor Classification Scheme Applied to the French X-, C-, and S-Band Polarimetric Radars, *Journal of Applied Meteorology and Climatology*, 52, 2328–2344, <https://doi.org/10.1175/JAMC-D-12-0236.1>, 2013.
- 555 Aldana, M.: Raw radar data and KDP dataset, <https://doi.org/10.57707/fmi-b2share.4126c5db27d24ddeae10d5c3163ff95a>, 2024.
- Andrić, J., Kumjian, M. R., Zrnić, D. S., Straka, J. M., and Melnikov, V. M.: Polarimetric Signatures above the Melting Layer in Winter Storms: An Observational and Modeling Study, *Journal of Applied Meteorology and Climatology*, 52, 682–700, <https://doi.org/10.1175/JAMC-D-12-028.1>, 2013.
- Bechini, R. and Chandrasekar, V.: A Semisupervised Robust Hydrometeor Classification Method for Dual-Polarization Radar Applications, *Journal of Atmospheric and Oceanic Technology*, 32, 22–47, <https://doi.org/10.1175/JTECH-D-14-00097.1>, 2015.
- 560 Besic, N., Figueras I Ventura, J., Grazioli, J., Gabella, M., Germann, U., and Berne, A.: Hydrometeor classification through statistical clustering of polarimetric radar measurements: a semi-supervised approach, *Atmos. Meas. Tech.*, 9, 4425–4445, <https://doi.org/10.5194/amt-9-4425-2016>, 2016.
- Blevins, B.: Losses due to rain on radomes and antenna reflecting surfaces, *IEEE Trans. Antennas Propagat.*, 13, 175–176, <https://doi.org/10.1109/TAP.1965.1138384>, 1965.
- 565 Boodoo, S., Hudak, D., Donaldson, N., and Leduc, M.: Application of Dual-Polarization Radar Melting-Layer Detection Algorithm, *Journal of Applied Meteorology and Climatology*, 49, 1779–1793, <https://doi.org/10.1175/2010JAMC2421.1>, 2010.
- Brandes, E. A., Zhang, G., and Vivekanandan, J.: Experiments in Rainfall Estimation with a Polarimetric Radar in a Subtropical Environment, *J. Appl. Meteor.*, 41, 674–685, [https://doi.org/10.1175/1520-0450\(2002\)041<0674:EIREWA>2.0.CO;2](https://doi.org/10.1175/1520-0450(2002)041<0674:EIREWA>2.0.CO;2), 2002.
- 570 Bringi, V., Thurai, M., Nakagawa, K., Huang, G., Kobayashi, T., Adachi, A., Hanado, H., and Sekizawa, S.: Rainfall Estimation from C-Band Polarimetric Radar in Okinawa, Japan: Comparisons with 2D-Video Disdrometer and 400 MHz Wind Profiler, *Journal of the Meteorological Society of Japan*, 84, 705–724, <https://doi.org/10.2151/jmsj.84.705>, 2006.
- Bringi, V. N. and Chandrasekar, V.: *Polarimetric Doppler weather radar: principles and applications*, Cambridge University Press, Cambridge, oCLC: 934243039, 2001.
- 575 Bringi, V. N., Rico-Ramirez, M. A., and Thurai, M.: Rainfall Estimation with an Operational Polarimetric C-Band Radar in the United Kingdom: Comparison with a Gauge Network and Error Analysis, *Journal of Hydrometeorology*, 12, 935–954, <https://doi.org/10.1175/JHM-D-10-05013.1>, 2011.
- Carey, L. D., Rutledge, S. A., Ahijevych, D. A., and Keenan, T. D.: Correcting Propagation Effects in C-Band Polarimetric Radar Observations of Tropical Convection Using Differential Propagation Phase, *J. Appl. Meteor.*, 39, 1405–1433, [https://doi.org/10.1175/1520-0450\(2000\)039<1405:CPEICB>2.0.CO;2](https://doi.org/10.1175/1520-0450(2000)039<1405:CPEICB>2.0.CO;2), 2000.
- 580 Chandrasekar, V., Bringi, V. N., Balakrishnan, N., and Zrnić, D. S.: Error Structure of Multiparameter Radar and Surface Measurements of Rainfall. Part III: Specific Differential Phase, *J. Atmos. Oceanic Technol.*, 7, 621–629, [https://doi.org/10.1175/1520-0426\(1990\)007<0621:ESOMRA>2.0.CO;2](https://doi.org/10.1175/1520-0426(1990)007<0621:ESOMRA>2.0.CO;2), 1990.
- Chandrasekar, V., Keränen, R., Lim, S., and Moisseev, D.: Recent advances in classification of observations from dual polarization weather radars, *Atmospheric Research*, 119, 97–111, <https://doi.org/10.1016/j.atmosres.2011.08.014>, 2013.
- 585 Chen, H. and Chandrasekar, V.: The quantitative precipitation estimation system for Dallas–Fort Worth (DFW) urban remote sensing network, *Journal of Hydrology*, 531, 259–271, <https://doi.org/10.1016/j.jhydrol.2015.05.040>, 2015.



- Chen, H., Chandrasekar, V., and Bechini, R.: An Improved Dual-Polarization Radar Rainfall Algorithm (DROPS2.0): Application in NASA IFloodS Field Campaign, *Journal of Hydrometeorology*, 18, 917–937, <https://doi.org/10.1175/JHM-D-16-0124.1>, 2017.
- 590 Cifelli, R., Chandrasekar, V., Lim, S., Kennedy, P. C., Wang, Y., and Rutledge, S. A.: A New Dual-Polarization Radar Rainfall Algorithm: Application in Colorado Precipitation Events, *Journal of Atmospheric and Oceanic Technology*, 28, 352–364, <https://doi.org/10.1175/2010JTECHA1488.1>, 2011.
- Cremonini, R., Voormansik, T., Post, P., and Moisseev, D.: Estimation of extreme precipitation events in Estonia and Italy using dual-polarization weather radar quantitative precipitation estimations, *Atmos. Meas. Tech.*, 16, 2943–2956, [https://doi.org/10.5194/amt-16-](https://doi.org/10.5194/amt-16-2943-2023)  
595 2943-2023, 2023.
- Dolan, B. and Rutledge, S. A.: A Theory-Based Hydrometeor Identification Algorithm for X-Band Polarimetric Radars, *Journal of Atmospheric and Oceanic Technology*, 26, 2071–2088, <https://doi.org/10.1175/2009JTECHA1208.1>, 2009.
- Dolan, B., Rutledge, S. A., Lim, S., Chandrasekar, V., and Thurai, M.: A Robust C-Band Hydrometeor Identification Algorithm and Application to a Long-Term Polarimetric Radar Dataset, *Journal of Applied Meteorology and Climatology*, 52, 2162–2186,  
600 <https://doi.org/10.1175/JAMC-D-12-0275.1>, 2013.
- Du, M., Gao, J., Zhang, G., Wang, Y., Heiselman, P. L., and Cui, C.: Assimilation of Polarimetric Radar Data in Simulation of a Supercell Storm with a Variational Approach and the WRF Model, *Remote Sensing*, 13, 3060, <https://doi.org/10.3390/rs13163060>, 2021.
- Giangrande, S. E. and Ryzhkov, A. V.: Estimation of Rainfall Based on the Results of Polarimetric Echo Classification, *Journal of Applied Meteorology and Climatology*, 47, 2445–2462, <https://doi.org/10.1175/2008JAMC1753.1>, 2008.
- 605 Giangrande, S. E., Krause, J. M., and Ryzhkov, A. V.: Automatic Designation of the Melting Layer with a Polarimetric Prototype of the WSR-88D Radar, *Journal of Applied Meteorology and Climatology*, 47, 1354–1364, <https://doi.org/10.1175/2007JAMC1634.1>, 2008.
- Giangrande, S. E., McGraw, R., and Lei, L.: An Application of Linear Programming to Polarimetric Radar Differential Phase Processing, *Journal of Atmospheric and Oceanic Technology*, 30, 1716–1729, <https://doi.org/10.1175/JTECH-D-12-00147.1>, 2013.
- Goddard, J., Tan, J., and Thurai, M.: Technique for calibration of meteorological radars using differential phase, *Electronics Letters*, 30,  
610 166–167, <https://doi.org/10.1049/el:19940119>, 1994.
- Gorgucci, E., Scarchilli, G., and Chandrasekar, V.: Calibration of radars using polarimetric techniques, *IEEE Trans. Geosci. Remote Sensing*, 30, 853–858, <https://doi.org/10.1109/36.175319>, 1992.
- Gourley, J. J., Illingworth, A. J., and Tabary, P.: Absolute Calibration of Radar Reflectivity Using Redundancy of the Polarization Observations and Implied Constraints on Drop Shapes, *Journal of Atmospheric and Oceanic Technology*, 26, 689–703,  
615 <https://doi.org/10.1175/2008JTECHA1152.1>, 2009.
- Grazioli, J., Tuia, D., and Berne, A.: Hydrometeor classification from polarimetric radar measurements: a clustering approach, *Atmos. Meas. Tech.*, 8, 149–170, <https://doi.org/10.5194/amt-8-149-2015>, 2015.
- Heistermann, M., Jacobi, S., and Pfaff, T.: Technical Note: An open source library for processing weather radar data (<i>wradlib</i>), *Hydrol. Earth Syst. Sci.*, 17, 863–871, <https://doi.org/10.5194/hess-17-863-2013>, 2013.
- 620 Helmus, J. J. and Collis, S. M.: The Python ARM Radar Toolkit (Py-ART), a Library for Working with Weather Radar Data in the Python Programming Language, *JORS*, 4, 25, <https://doi.org/10.5334/jors.119>, 2016.
- Hickman, B.: Precipitation estimation in urban areas by employing a dense-network of weather radars, M.Sci Thesis, University of Helsinki, Helsinki, <http://urn.fi/URN:NBN:fi-fe2017112251840>, 2015.
- Holleman, I., Huuskonen, A., and Taylor, B.: Solar Monitoring of the NEXRAD WSR-88D Network Using Operational Scan Data, *Journal of Atmospheric and Oceanic Technology*, 39, 125–139, <https://doi.org/10.1175/JTECH-D-20-0204.1>, 2022.  
625



- Huang, H., Zhang, G., Zhao, K., and Giangrande, S. E.: A Hybrid Method to Estimate Specific Differential Phase and Rainfall With Linear Programming and Physics Constraints, *IEEE Trans. Geosci. Remote Sensing*, 55, 96–111, <https://doi.org/10.1109/TGRS.2016.2596295>, 2017.
- Hubbert, J. and Bringi, V. N.: An Iterative Filtering Technique for the Analysis of Copolar Differential Phase and Dual-Frequency Radar Measurements, *J. Atmos. Oceanic Technol.*, 12, 643–648, [https://doi.org/10.1175/1520-0426\(1995\)012<0643:AIFTFT>2.0.CO;2](https://doi.org/10.1175/1520-0426(1995)012<0643:AIFTFT>2.0.CO;2), 1995.
- Hubbert, J., Chandrasekar, V., Bringi, V. N., and Meischner, P.: Processing and Interpretation of Coherent Dual-Polarized Radar Measurements, *J. Atmos. Oceanic Technol.*, 10, 155–164, [https://doi.org/10.1175/1520-0426\(1993\)010<0155:PAIOCD>2.0.CO;2](https://doi.org/10.1175/1520-0426(1993)010<0155:PAIOCD>2.0.CO;2), 1993.
- Huuskonen, A. and Holleman, I.: Determining Weather Radar Antenna Pointing Using Signals Detected from the Sun at Low Antenna Elevations, *Journal of Atmospheric and Oceanic Technology*, 24, 476–483, <https://doi.org/10.1175/JTECH1978.1>, 2007.
- 635 I. Mishchenko, M., Travis, L. D., and Macke, A.: T-Matrix Method and Its Applications, in: *Light Scattering by Nonspherical Particles*, pp. 147–172, Elsevier, <https://doi.org/10.1016/B978-012498660-2/50033-1>, 2000.
- Illingworth, A.: Improved Precipitation Rates and Data Quality by Using Polarimetric Measurements, in: *Weather Radar*, edited by Guzzi, R., Imboden, D., Lanzerotti, L. J., Platt, U., and Meischner, P., pp. 130–166, Springer Berlin Heidelberg, Berlin, Heidelberg, [https://doi.org/10.1007/978-3-662-05202-0\\_5](https://doi.org/10.1007/978-3-662-05202-0_5), 2004.
- 640 Illingworth, A. J. and Blackman, T. M.: The Need to Represent Raindrop Size Spectra as Normalized Gamma Distributions for the Interpretation of Polarization Radar Observations, *J. Appl. Meteor.*, 41, 286–297, [https://doi.org/10.1175/1520-0450\(2002\)041<0286:TNTRRS>2.0.CO;2](https://doi.org/10.1175/1520-0450(2002)041<0286:TNTRRS>2.0.CO;2), 2002.
- Keenan, T. D.: Hydrometeor classification with a C-Band polarimetric radar, *Australian Meteorological Magazine*, 52, 23–31, 2003.
- Kennedy, P. C. and Rutledge, S. A.: S-Band Dual-Polarization Radar Observations of Winter Storms, *Journal of Applied Meteorology and*
- 645 *Climatology*, 50, 844–858, <https://doi.org/10.1175/2010JAMC2558.1>, 2011.
- Kumjian, M.: Principles and applications of dual-polarization weather radar. Part III: Artifacts, *J. Operational Meteor.*, 1, 265–274, <https://doi.org/10.15191/nwajom.2013.0121>, 2013.
- Kumjian, M. R.: Weather Radars, in: *Remote Sensing of Clouds and Precipitation*, edited by Andronache, C., pp. 15–63, Springer International Publishing, Cham, [https://doi.org/10.1007/978-3-319-72583-3\\_2](https://doi.org/10.1007/978-3-319-72583-3_2), series Title: Springer Remote Sensing/Photogrammetry, 2018.
- 650 Kumjian, M. R. and Lombardo, K. A.: Insights into the Evolving Microphysical and Kinematic Structure of Northeastern U.S. Winter Storms from Dual-Polarization Doppler Radar, *Mon. Wea. Rev.*, 145, 1033–1061, <https://doi.org/10.1175/MWR-D-15-0451.1>, 2017.
- Kumjian, M. R., Lebo, Z. J., and Ward, A. M.: Storms Producing Large Accumulations of Small Hail, *Journal of Applied Meteorology and Climatology*, 58, 341–364, <https://doi.org/10.1175/JAMC-D-18-0073.1>, 2019.
- Kurri, M. and Huuskonen, A.: Measurements of the Transmission Loss of a Radome at Different Rain Intensities, *Journal of Atmospheric*
- 655 *and Oceanic Technology*, 25, 1590–1599, <https://doi.org/10.1175/2008JTECHA1056.1>, 2008.
- Leinonen, J.: High-level interface to T-matrix scattering calculations: architecture, capabilities and limitations, *Opt. Express*, 22, 1655, <https://doi.org/10.1364/OE.22.001655>, 2014.
- Leinonen, J., Moisseev, D., Leskinen, M., and Petersen, W. A.: A Climatology of Disdrometer Measurements of Rainfall in Finland over Five Years with Implications for Global Radar Observations, *Journal of Applied Meteorology and Climatology*, 51, 392–404, <https://doi.org/10.1175/JAMC-D-11-056.1>, 2012.
- 660 Li, H., Moisseev, D., Luo, Y., Liu, L., Ruan, Z., Cui, L., and Bao, X.: Assessing specific differential phase ( $K_{DP}$ )-based quantitative precipitation estimation for the record-breaking rainfall over Zhengzhou city on 20 July 2021, *Hydrol. Earth Syst. Sci.*, 27, 1033–1046, <https://doi.org/10.5194/hess-27-1033-2023>, 2023.



- 665 Lim, S., Chandrasekar, V., and Bringi, V.: Hydrometeor classification system using dual-polarization radar measurements: model improve-  
ments and in situ verification, *IEEE Trans. Geosci. Remote Sensing*, 43, 792–801, <https://doi.org/10.1109/TGRS.2004.843077>, 2005.
- Liu, H. and Chandrasekar, V.: Classification of Hydrometeors Based on Polarimetric Radar Measurements: Development of Fuzzy  
Logic and Neuro-Fuzzy Systems, and In Situ Verification, *J. Atmos. Oceanic Technol.*, 17, 140–164, [https://doi.org/10.1175/1520-0426\(2000\)017<0140:COHBOP>2.0.CO;2](https://doi.org/10.1175/1520-0426(2000)017<0140:COHBOP>2.0.CO;2), 2000.
- 670 Maesaka, T., Iwanami, K., and Maki, M.: Non-negative KDP Estimation by Monotone Increasing  $\Phi$ DP Assumption below Melting Layer,  
p. 6, 2012.
- Marzano, F. S., Scaranari, D., and Vulpiani, G.: Supervised Fuzzy-Logic Classification of Hydrometeors Using C-Band Weather Radars,  
*IEEE Trans. Geosci. Remote Sensing*, 45, 3784–3799, <https://doi.org/10.1109/TGRS.2007.903399>, 2007.
- Matrosov, S. Y., Cifelli, R., Kennedy, P. C., Nesbitt, S. W., Rutledge, S. A., Bringi, V. N., and Martner, B. E.: A Comparative Study of  
675 Rainfall Retrievals Based on Specific Differential Phase Shifts at X- and S-Band Radar Frequencies, *Journal of Atmospheric and Oceanic  
Technology*, 23, 952–963, <https://doi.org/10.1175/JTECH1887.1>, 2006.
- May, P. T., Keenan, T. D., Zrnić, D. S., Carey, L. D., and Rutledge, S. A.: Polarimetric Radar Measurements of Tropical Rain at a 5-cm  
Wavelength, *J. Appl. Meteor.*, 38, 750–765, [https://doi.org/10.1175/1520-0450\(1999\)038<0750:PRMOTR>2.0.CO;2](https://doi.org/10.1175/1520-0450(1999)038<0750:PRMOTR>2.0.CO;2), 1999.
- Moisseev, D. N.: FMI Parsivel23, <https://hdl.handle.net/21.12132/3.69dddc0004b64b32>, 2024.
- Moisseev, D. N., Lautaportti, S., Tyynela, J., and Lim, S.: Dual-polarization radar signatures in snowstorms: Role of snowflake aggregation,  
680 *JGR Atmospheres*, 120, 12 644–12 655, <https://doi.org/10.1002/2015JD023884>, 2015.
- Otto, T. and Russchenberg, H. W. J.: Estimation of Specific Differential Phase and Differential Backscatter Phase From Polarimetric Weather  
Radar Measurements of Rain, *IEEE Geosci. Remote Sensing Lett.*, 8, 988–992, <https://doi.org/10.1109/LGRS.2011.2145354>, 2011.
- Oue, M., Kumjian, M. R., Lu, Y., Jiang, Z., Clothiaux, E. E., Verlinde, J., and Aydin, K.: X-Band Polarimetric and Ka-Band Doppler Spectral  
685 Radar Observations of a Graupel-Producing Arctic Mixed-Phase Cloud, *Journal of Applied Meteorology and Climatology*, 54, 1335–1351,  
<https://doi.org/10.1175/JAMC-D-14-0315.1>, 2015.
- Park, H. S., Ryzhkov, A. V., Zrnić, D. S., and Kim, K.-E.: The Hydrometeor Classification Algorithm for the Polarimetric WSR-88D:  
Description and Application to an MCS, *Weather and Forecasting*, 24, 730–748, <https://doi.org/10.1175/2008WAF2222205.1>, 2009.
- Ramdas, A., Garcia, N., and Cuturi, M.: On Wasserstein Two Sample Testing and Related Families of Nonparametric Tests,  
<https://doi.org/10.48550/ARXIV.1509.02237>, version Number: 2, 2015.
- 690 Reimel, K. J. and Kumjian, M.: Evaluation of KDP Estimation Algorithm Performance in Rain Using a Known-Truth Framework, *Journal  
of Atmospheric and Oceanic Technology*, 38, 587–605, <https://doi.org/10.1175/JTECH-D-20-0060.1>, 2021.
- Reinoso-Rondinel, R., Unal, C., and Russchenberg, H.: Adaptive and High-Resolution Estimation of Specific Differential Phase for Polari-  
metric X-Band Weather Radars, *Journal of Atmospheric and Oceanic Technology*, 35, 555–573, <https://doi.org/10.1175/JTECH-D-17-0105.1>, 2018.
- 695 Ribaud, J.-F., Machado, L. A. T., and Biscaro, T.: X-band dual-polarization radar-based hydrometeor classification for Brazilian tropical  
precipitation systems, *Atmos. Meas. Tech.*, 12, 811–837, <https://doi.org/10.5194/amt-12-811-2019>, 2019.
- Ryzhkov, A. and Zrnic, D.: Beamwidth Effects on the Differential Phase Measurements of Rain, *J. Atmos. Oceanic Technol.*, 15, 624–634,  
[https://doi.org/10.1175/1520-0426\(1998\)015<0624:BEOTDP>2.0.CO;2](https://doi.org/10.1175/1520-0426(1998)015<0624:BEOTDP>2.0.CO;2), 1998.
- Ryzhkov, A. and Zrnić, D.: Assessment of Rainfall Measurement That Uses Specific Differential Phase, *J. Appl. Meteor.*, 35, 2080–2090,  
700 [https://doi.org/10.1175/1520-0450\(1996\)035<2080:AORMTU>2.0.CO;2](https://doi.org/10.1175/1520-0450(1996)035<2080:AORMTU>2.0.CO;2), 1996.





- Ryzhkov, A. V. and Zrníc, D. S.: Radar Polarimetry for Weather Observations, Springer Atmospheric Sciences, Springer International Publishing : Imprint: Springer, Cham, 1st ed. 2019 edn., <https://doi.org/10.1007/978-3-030-05093-1>, 2019.
- Ryzhkov, A. V. and Zrníc, D. S.: Comparison of Dual-Polarization Radar Estimators of Rain, *J. Atmos. Oceanic Technol.*, 12, 249–256, [https://doi.org/10.1175/1520-0426\(1995\)012<0249:CODPRE>2.0.CO;2](https://doi.org/10.1175/1520-0426(1995)012<0249:CODPRE>2.0.CO;2), 1995.
- 705 Ryzhkov, A. V., Giangrande, S. E., Melnikov, V. M., and Schuur, T. J.: Calibration Issues of Dual-Polarization Radar Measurements, *Journal of Atmospheric and Oceanic Technology*, 22, 1138–1155, <https://doi.org/10.1175/JTECH1772.1>, 2005a.
- Ryzhkov, A. V., Giangrande, S. E., and Schuur, T. J.: Rainfall Estimation with a Polarimetric Prototype of WSR-88D, *Journal of Applied Meteorology*, 44, 502–515, <https://doi.org/10.1175/JAM2213.1>, 2005b.
- Ryzhkov, A. V., Schuur, T. J., Burgess, D. W., Heinselman, P. L., Giangrande, S. E., and Zrníc, D. S.: The Joint Polarization Experiment: Polarimetric Rainfall Measurements and Hydrometeor Classification, *Bull. Amer. Meteor. Soc.*, 86, 809–824, <https://doi.org/10.1175/BAMS-86-6-809>, 2005c.
- 710 Sachidananda, M. and Zrníc, D. S.: Rain Rate Estimates from Differential Polarization Measurements, *J. Atmos. Oceanic Technol.*, 4, 588–598, [https://doi.org/10.1175/1520-0426\(1987\)004<0588:RREFDP>2.0.CO;2](https://doi.org/10.1175/1520-0426(1987)004<0588:RREFDP>2.0.CO;2), 1987.
- Schneebeli, M. and Berne, A.: An Extended Kalman Filter Framework for Polarimetric X-Band Weather Radar Data Processing, *Journal of Atmospheric and Oceanic Technology*, 29, 711–730, <https://doi.org/10.1175/JTECH-D-10-05053.1>, 2012.
- 715 Schneebeli, M., Dawes, N., Lehning, M., and Berne, A.: High-Resolution Vertical Profiles of X-Band Polarimetric Radar Observables during Snowfall in the Swiss Alps, *Journal of Applied Meteorology and Climatology*, 52, 378–394, <https://doi.org/10.1175/JAMC-D-12-015.1>, 2013.
- Schneebeli, M., Grazioli, J., and Berne, A.: Improved Estimation of the Specific Differential Phase Shift Using a Compilation of Kalman Filter Ensembles, *IEEE Trans. Geosci. Remote Sensing*, 52, 5137–5149, <https://doi.org/10.1109/TGRS.2013.2287017>, 2014.
- 720 Snyder, J. C., Bluestein, H. B., Zhang, G., and Frasier, S. J.: Attenuation Correction and Hydrometeor Classification of High-Resolution, X-band, Dual-Polarized Mobile Radar Measurements in Severe Convective Storms, *Journal of Atmospheric and Oceanic Technology*, 27, 1979–2001, <https://doi.org/10.1175/2010JTECHA1356.1>, 2010.
- Tapping, K. F.: The 10.7 cm solar radio flux ( $F_{10.7}$ ), *Space Weather*, 11, 394–406, <https://doi.org/10.1002/swe.20064>, 2013.
- 725 Tessendorf, S. A., Miller, L. J., Wiens, K. C., and Rutledge, S. A.: The 29 June 2000 Supercell Observed during STEPS. Part I: Kinematics and Microphysics, *Journal of the Atmospheric Sciences*, 62, 4127–4150, <https://doi.org/10.1175/JAS3585.1>, 2005.
- Thomas, G., Mahfouf, J.-F., and Montmerle, T.: Toward a variational assimilation of polarimetric radar observations in a convective-scale numerical weather prediction (NWP) model, *Atmos. Meas. Tech.*, 13, 2279–2298, <https://doi.org/10.5194/amt-13-2279-2020>, 2020.
- Thompson, E. J., Rutledge, S. A., Dolan, B., Chandrasekar, V., and Cheong, B. L.: A Dual-Polarization Radar Hydrometeor Classification Algorithm for Winter Precipitation, *Journal of Atmospheric and Oceanic Technology*, 31, 1457–1481, <https://doi.org/10.1175/JTECH-D-13-00119.1>, 2014.
- 730 Thompson, E. J., Rutledge, S. A., Dolan, B., Thurai, M., and Chandrasekar, V.: Dual-Polarization Radar Rainfall Estimation over Tropical Oceans, *Journal of Applied Meteorology and Climatology*, 57, 755–775, <https://doi.org/10.1175/JAMC-D-17-0160.1>, 2018.
- Thurai, M. and Bringi, V. N.: Drop Axis Ratios from a 2D Video Disdrometer, *Journal of Atmospheric and Oceanic Technology*, 22, 966–978, <https://doi.org/10.1175/JTECH1767.1>, 2005.
- 735 Thurai, M., Huang, G. J., Bringi, V. N., Randeu, W. L., and Schönhuber, M.: Drop Shapes, Model Comparisons, and Calculations of Polarimetric Radar Parameters in Rain, *J. Atmos. Oceanic Technol.*, 24, 1019–1032, <https://doi.org/10.1175/JTECH2051.1>, 2007.



- Tiira, J. and Moisseev, D.: Unsupervised classification of vertical profiles of dual polarization radar variables, *Atmos. Meas. Tech.*, 13, 1227–1241, <https://doi.org/10.5194/amt-13-1227-2020>, 2020.
- 740 Vaisala: IRIS (version 8.13), [www.vaisala.com](http://www.vaisala.com), 2017.
- Virtanen, P., Gommers, R., Oliphant, T. E., Haberland, M., Reddy, T., Cournapeau, D., Burovski, E., Peterson, P., Weckesser, W., Bright, J., van der Walt, S. J., Brett, M., Wilson, J., Millman, K. J., Mayorov, N., Nelson, A. R. J., Jones, E., Kern, R., Larson, E., Carey, C. J., Polat, İ., Feng, Y., Moore, E. W., VanderPlas, J., Laxalde, D., Perktold, J., Cimrman, R., Henriksen, I., Quintero, E. A., Harris, C. R., Archibald, A. M., Ribeiro, A. H., Pedregosa, F., van Mulbregt, P., and SciPy 1.0 Contributors: SciPy 1.0: Fundamental Algorithms for Scientific Computing in Python, *Nature Methods*, 17, 261–272, <https://doi.org/10.1038/s41592-019-0686-2>, 2020.
- 745 Vivekanandan, J., Ellis, S. M., Oye, R., Zrníc, D. S., Ryzhkov, A. V., and Straka, J.: Cloud Microphysics Retrieval Using S-band Dual-Polarization Radar Measurements, *Bull. Amer. Meteor. Soc.*, 80, 381–388, [https://doi.org/10.1175/1520-0477\(1999\)080<0381:CMRUSB>2.0.CO;2](https://doi.org/10.1175/1520-0477(1999)080<0381:CMRUSB>2.0.CO;2), 1999.
- Vivekanandan, J., Zhang, G., Ellis, S. M., Rajopadhyaya, D., and Avery, S. K.: Radar reflectivity calibration using differential propagation phase measurement: RADAR REFLECTIVITY CALIBRATION, *Radio Sci.*, 38, n/a–n/a, <https://doi.org/10.1029/2002RS002676>, 2003.
- 750 Vulpiani, G., Montopoli, M., Passeri, L. D., Gioia, A. G., Giordano, P., and Marzano, F. S.: On the Use of Dual-Polarized C-Band Radar for Operational Rainfall Retrieval in Mountainous Areas, *Journal of Applied Meteorology and Climatology*, 51, 405–425, <https://doi.org/10.1175/JAMC-D-10-05024.1>, 2012.
- Wang, Y. and Chandrasekar, V.: Algorithm for Estimation of the Specific Differential Phase, *Journal of Atmospheric and Oceanic Technology*, 26, 2565–2578, <https://doi.org/10.1175/2009JTECHA1358.1>, 2009.
- 755 Wang, Y., Zhang, J., Ryzhkov, A. V., and Tang, L.: C-Band Polarimetric Radar QPE Based on Specific Differential Propagation Phase for Extreme Typhoon Rainfall, *Journal of Atmospheric and Oceanic Technology*, 30, 1354–1370, <https://doi.org/10.1175/JTECH-D-12-00083.1>, 2013.
- Waterman, P.: Matrix formulation of electromagnetic scattering, *Proc. IEEE*, 53, 805–812, <https://doi.org/10.1109/PROC.1965.4058>, 1965.
- 760 Wen, G., Protat, A., May, P. T., Wang, X., and Moran, W.: A Cluster-Based Method for Hydrometeor Classification Using Polarimetric Variables. Part I: Interpretation and Analysis, *Journal of Atmospheric and Oceanic Technology*, 32, 1320–1340, <https://doi.org/10.1175/JTECH-D-13-00178.1>, 2015.
- Wen, G., Fox, N. I., and Market, P. S.: A Gaussian mixture method for specific differential phase retrieval at X-band frequency, *Atmos. Meas. Tech.*, 12, 5613–5637, <https://doi.org/10.5194/amt-12-5613-2019>, 2019.
- 765 Zhang, J., Tang, L., Cocks, S., Zhang, P., Ryzhkov, A., Howard, K., Langston, C., and Kaney, B.: A Dual-Polarization Radar Synthetic QPE for Operations, *Journal of Hydrometeorology*, 21, 2507–2521, <https://doi.org/10.1175/JHM-D-19-0194.1>, 2020.
- Zrníc, D. S. and Ryzhkov, A.: Advantages of Rain Measurements Using Specific Differential Phase, *J. Atmos. Oceanic Technol.*, 13, 454–464, [https://doi.org/10.1175/1520-0426\(1996\)013<0454:AORMUS>2.0.CO;2](https://doi.org/10.1175/1520-0426(1996)013<0454:AORMUS>2.0.CO;2), 1996.
- Zrníc, D. S., Ryzhkov, A., Straka, J., Liu, Y., and Vivekanandan, J.: Testing a Procedure for Automatic Classification of Hydrometeor Types, *J. Atmos. Oceanic Technol.*, 18, 892–913, [https://doi.org/10.1175/1520-0426\(2001\)018<0892:TAPFAC>2.0.CO;2](https://doi.org/10.1175/1520-0426(2001)018<0892:TAPFAC>2.0.CO;2), 2001.
- 770